Applied Energy 335 (2023) 120743

Contents lists available at ScienceDirect

Applied Energy

journal homepage: www.elsevier.com/locate/apenergy

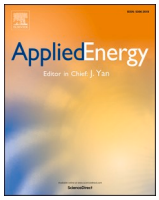

Thermal performance analysis and experimental verification of lithium-ion batteries for electric vehicle applications through optimized inclined mini-channels

Ashima Verma [a], Tanmoy Saikia [b], Pranaynil Saikia [c,*], Dibakar Rakshit [a,d,*], Carlos E. Ugalde-Loo [c]

[a] Department of Energy Science and Engineering, Indian Institute of Technology Delhi, Hauz Khas, New Delhi, India
[b] Department of Electrical Engineering, Jorhat Engineering College, Assam, India
[c] School of Engineering, Cardiff University, Wales, United Kingdom
[d] Honorary Associate Professor, The University of Queensland, Australia

HIGHLIGHTS

- Investigation of the thermal performance of coolant mini-channels in a Li-ion battery.
- A realistic driving cycle is considered for the thermal performance analysis.
- An experimentally validated battery model is used for the parametric study.
- Analysis of power consumption by the active battery cooling technology.
- Optimal cooling system design is selected based on multicriteria decision-making.

ARTICLE INFO

Keywords:
Battery thermal management system
Electric vehicle
Liquid cooling
Mini-channel
Parasitic power consumption
Real-time driving cycle

ABSTRACT

Power units (i.e., batteries) of electric vehicles (EVs) generate heat while being charged or discharged, which deteriorates their performance and reliability over time. This paper investigates a comprehensive spectrum of geometric and thermo-fluidic parameters of a liquid coolant flowing through mini-channels. These are embedded in the surface of an EV battery to curtail overheating. Design parameters such as aspect ratio and angular orientation of the mini-channels were varied randomly to investigate several geometric configurations that are scarcely intuitive. The coolant mass flow rate and the fluid inlet temperature were also varied through a large dataset of randomly distributed values. A real-time EV driving cycle was implemented alongside an experimentally validated model to evaluate the battery operation, which evidenced the complex dependence of the battery's thermal state with different levels of cooling retrofitting. The study also analyzed the parasitic power consumption arising from the pumping and cooling energy demands to drive the coolant system to achieve an optimally designed retrofit for a reliable battery performance. It was found that the mini-channel parameters considerably affect the thermal performance of the battery. However, the optimized case was found to have a minimum temperature difference in the battery and a minimum power requirement. The case with a fluid inlet velocity of 0.13 m/s, a fluid inlet temperature of 312.9 K, an aspect ratio of 1.7, and an inclination angle of 4.9° was found to be the most suitable, leading to a refrigeration power requirement of 0.85 W only. The battery temperature after the end of the driving cycle was maintained at 313 K.

1. Introduction

Vehicular transport supported through sustainably sourced electricity is a prominently explored alternative to address climate change concerns. For example, the 7th of the Sustainable Development Goals by the United Nations (UN report, 2015) focuses on affordable and clean energy. It includes the development of the modern renewable

* Corresponding authors.
E-mail addresses: SaikiaP@cardiff.ac.uk (P. Saikia), dibakar@iitd.ac.in (D. Rakshit).

https://doi.org/10.1016/j.apenergy.2023.120743
Received 22 October 2022; Received in revised form 26 December 2022; Accepted 20 January 2023
Available online 7 February 2023

Nomenclature and variables

Abbreviation / Variable	Meaning
ACS	active cooling system
BTMS	battery thermal management system
CFD	computational fluid dynamics
COP	coefficient of performance
CPCM	composite phase change material
DOD	depth of discharge
DOE	design of experiments
EV	electric vehicle
HCS	hybrid cooling system
LHS	Latin hypercube sampling
Li-ion	lithium-ion
MSMD	multi-scale multi-dimensional
NTGK	Newman, Tiedemann, Gu, and Kim
Nu	Nusselt number
PCM	phase change material
PCS	passive cooling system
Re	Reynolds number
ROM	reduced order method
TOPSIS	Technique for Order Preference by Similarity to an Ideal Solution
$\dot{q}$	heat generation rate during battery operation (W)
σ_-	effective electrical conductivity of the negative electrode (S/m)
σ_+	effective electrical conductivity of the positive electrode (S/m)
φ_-	phase potential for the negative electrode (V)
φ_+	phase potential for the positive electrode (V)
$\triangle P$	pressure drop (Pa)
$\triangle T$	temperature difference (K)
C_P	specific heat (J/kg-K)
D_h	hydraulic diameter (m)
f	friction factor
h	heat transfer coefficient (W/m^2-K)
i	mini-channel inclination angle (degree)
J	volumetric transfer for current density (A/m^2)
k	thermal conductivity (W/m-K)
l	width of mini-channel (m)
L	length of the pipe (m)
m	mass flow rate (kg/s)
Q	volumetric flow rate (m^3/s)
q	cooling load (W)
Q_{Ah}	battery capacity (Ah)
T	absolute temperature (K)
t_a	ambient temperature (K)
t_i	fluid inlet temperature (K)
t_{initial}	initial temperature (K)
V	volume of the battery (m^3)
v	fluid inlet velocity (m/s)
w	height or thickness of the mini-channel (m)
W_c	refrigeration work (W)
W_P	pumping power (W)
x	mini-channel aspect ratio
μ	dynamic viscosity (kg/m-s)
ρ	density (kg/m^3)

transport sector by 2030 [1]. Electric vehicles (EVs) have, therefore, emerged as the next generation option for transport.

The adoption of EVs curbs harmful greenhouse gas emissions of internal combustion engines and reduces noise pollution in metropolitan cities [2]. The conventional power unit of an EV is the lithium-ion (Li-ion) battery pack. These batteries have high energy densities (up to 705 Wh/L),high power densities (10,000 W/L), and low self-discharge rates [3].

Ambient conditions significantly influence the thermal performance of Li-ion batteries. For example, capacity fading is a common phenomenon exhibited at high ambient temperatures [4]. The acceptable operational range of these batteries is from 253 K to 333 K, but the optimum range lies within 288 K to 308 K (i.e., 15 °C to 35 °C) [5,6]. It has been reported that the thermal performance is critical at temperatures above 313 K and below 293 K [7]. This is because capacity degradation occurs above 313 K, and the internal resistance increases when the temperature drops below 293 K. Furthermore, the temperature difference between the cells of the battery pack must not exceed 5 K to guarantee an adequate thermal performance [8]. Thus, temperature non-uniformity is a threat to the state of health of the power unit [9]. Therefore, Li-ion batteries need management throughout the driving cycle in two ways: performance and heat management [10].

The thermal stress developed in a battery pack must be handled with utmost care to prevent thermal runaway. Thermal runaway is critical as it often results in uncontrolled fire hazards due to the production of flammable gases ensuing from the reaction between the negative electrode and the electrolyte [11]. It starts with the decomposition of the solid electrolyte interphase layer when the battery pack is over-charged, over-discharged, or if it is operated at a high ambient temperature. Thus, it is crucial to identify and limit the extent of thermal runaway as a safety measure. A battery thermal management system (BTMS) is required to achieve this.

BTMSs can be classified into four categories. The main two are active cooling systems (ACSs) and passive cooling systems (PCSs). A third category combines ACS with PCS and is known as a hybrid cooling system (HCS). An ACS utilizes air or liquid as the heat transfer medium, whereas a PCS relies on incorporating phase change materials (PCMs) and fins to dissipate heat. In recent years, immersion cooling has emerged as a new BTMS, where a non-conductive dielectric fluid (such as oil) in direct contact with the battery pack is used [12].

PCMs, which are the heat transfer media in PCSs, have been investigated as alternatives to ACSs in various references. This is because the high latent heat of a PCM may absorb efficiently the heat emitted by Li-ion batteries [13,14]. The performance can be further improved by enhancing the thermal conductivity of the PCM [15,16]. The influence of adding fins and the thermal performance of the PCM in extreme environments has been explained in detail in previous studies [17,18]. It was found in [19] that the extensive and intensive properties of the fins and PCM have a significant impact on the thermal performance of the battery and an optimized design can control the battery's temperature within the permissible limits. However, if the PCM runs out of its available latent heat at extreme operating conditions, the thermal management system may fail. Thus, a PCS requires additional provisions to support the cooling system in harsh operating conditions [20]. Ref. [21] is relevant, as it presents a study in which the mass and volume of the PCM were minimized using an optimization approach based on the response surface methodology. Such an approach represents a powerful tool to perform multi-objective optimization considering different constraints and system parameters [21].

Air cooling is a popular ACS which enables managing the maximum temperature in a battery pack. However, the thermal performance is not satisfactory at high ambient temperatures as air has a low thermal conductivity and a low specific heat [22]. In addition, the high flow rates represent a challenge and the space required for an air-cooled system is larger than for a liquid-cooled system. Conversely, the higher thermal conductivity and specific heat capacity afforded by liquid cooling

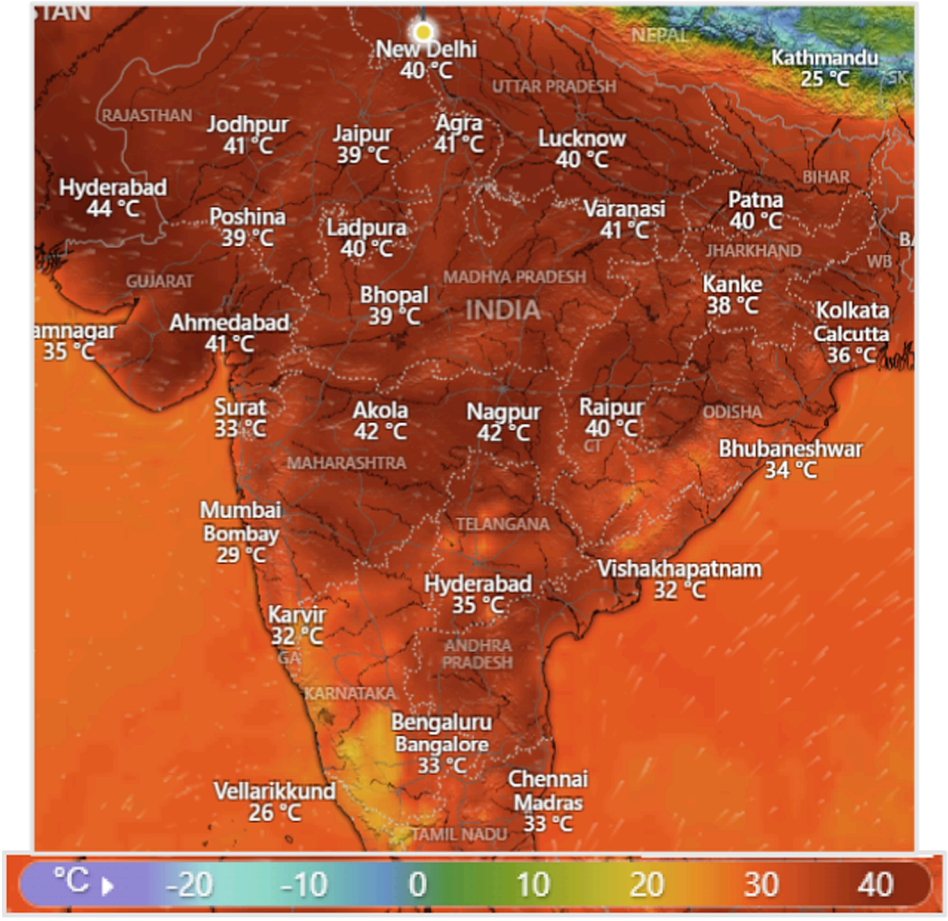

Fig. 1. Temperature distribution in India on 15 April 2022 at 4:00 pm [52].

Table 1
Input parameters.

Parameter	Lower bound	Upper bound
Fluid inlet velocity (v)	0.05 m/s	0.5 m/s
Fluid inlet temperature (t_i)	298 K	313 K
Mini-channel inclination angle (i)	0°	90°
Mini-channel aspect ratio (x)	1	10

systems is advantageous [23]. The importance of these systems for the efficient operation of a BTMS has been highlighted by some studies [24]. Among the available coolants for liquid-cooled battery packs, a commonly employed is the water/glycol solvent, where glycol is used to reduce the freezing point of water [25]. The study presented in [26] identified liquid cooling systems as more energy efficient than their air-cooled counterparts. For instance, for a 0.5 W power consumption, the temperature of the hottest cell in the battery pack of a liquid-cooled module was lower by 3 K than for an air-cooled module. Due to the high cooling efficiency and compact structure afforded by liquid-cooled battery packs, EV manufacturers such Tesla (Model S), Chevrolet (Bolt), and Audi (e-Tron) favor their use [27].

Wavy microchannels and microtubes, which constitute other types of ACS, may be used simultaneously with a biologically synthesized working nanofluid (e.g., silver-water/ethylene glycol, 50:50) to cool Li-ion batteries, as reported in [28]. In this reference, after completely discharging the battery at discharge rates of 1C, 2C, 4C, and 5C (where 1C implies that a fully charged battery rated at 1 Ah should provide 1 A for one hour [29]), the maximum temperature of the battery was maintained respectively at 305.6 K, 310.3 K, 321 K, and 326.7 K [28]. A magnetic pulsative nanofluid flow through the microchannels has been also employed for battery cooling [30]. The magnitude of the inlet velocity and the Reynolds number were the two parameters identified to impact the battery cooling. The effect of the velocity and temperature of the inlet water on a Li-ion battery pack at a 5C discharge rate was explored in [31]. The battery pack temperature was kept below 313 K. Results show that the temperature difference peaked when the inlet water temperature dropped from 293 K to 274 K.

Significant emphasis has been made on the design of mini-channels for battery packs to improve ACSs. For instance, the possibility of installing a cold plate with 5 mini-channels on a Li-ion battery pack was investigated in [32]. The study found that an inlet water temperature of 298 K and a mass flow rate of 3 g/s are ideal to maintain the battery pack within the temperature range of 298 K to 313 K for all climatic conditions. The flow pattern of the liquid also impacts the cooling provision. A unique U-turn cold plate with an alternative inlet and outlet crossflow arrangement enables a drop by 32.2% of the maximum temperature in comparison to a parallel-type arrangement, as shown in [33]. The shape of the mini-channels also impacts the battery cooling provision. For example, sine and sawtooth wave cross-sections exhibit a better thermal performance than the traditional rectangular mini-channels [34]. In another study, divergent-shaped channels with two inlets and one outlet were found to reduce the pressure drop by 7.2% and the maximum temperature by 0.8 K [35]. In addition, a counter-flow arrangement of coolant inside the mini-channels reduces the temperature difference within the battery.

The significance of the surface area covered with cold plates/channels was demonstrated in [36]. For instance, an enhanced heat transfer was enabled by zig-zag plates as they cover a larger surface area. In turn, this contributed to increasing the thermal performance of the battery module by 28%. The study reported in [37] demonstrated that the

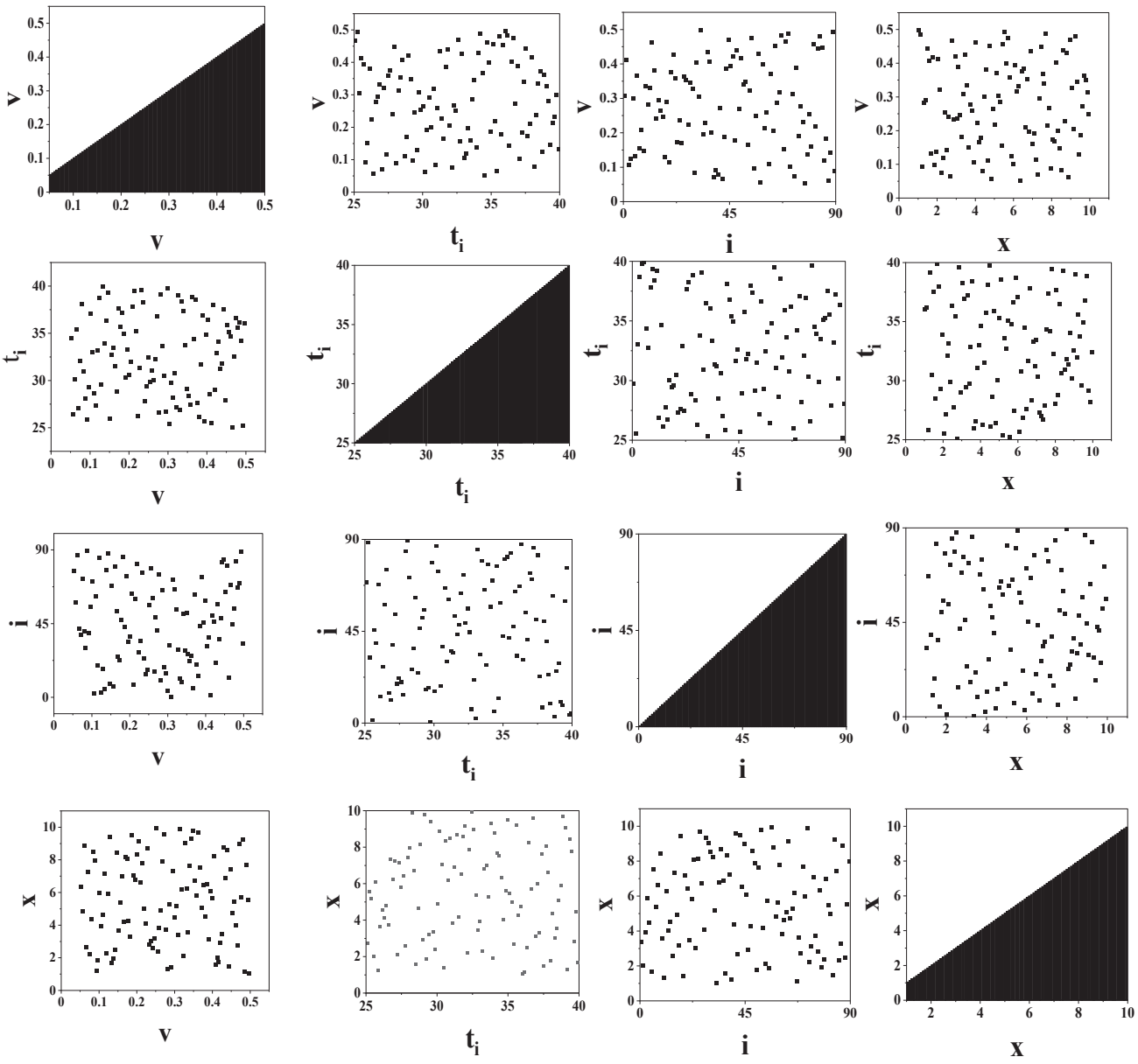

Fig. 2. Sample distribution of design variables through the LHS method.

thermal performance of a single cell can be improved by a cold plate retrofit with cooling water flowing through a two-way mini-channel. A parallel mini-channel cold plate was designed for large battery packs in [38]. The influence of the outlet design of the mini-channel was found to influence the thermal performance. An optimized design of the cold plate reduced the temperature difference by at least 76% and the pumping power by 81%. In [39], the Latin hypercube sampling (LHS) method was adopted to design serpentine cooling plates for battery cooling. Cooling channel parameters including the fluid inlet velocity, the Reynolds number, the channel dimensions, and the flow pattern were optimized for the best-case scenario. The average temperature decreased by 14% in comparison to the reference temperature.

In [40], the discharge rate, mass flow rate, fluid inlet temperature, and ambient temperature were identified as important input parameters for liquid cooling systems. In this reference three designs with heat pipes were presented, which increased the heat transfer area of the cooling system. The best case achieved a temperature drop of 9.4 K. The performance of parallel-spiral serpentine liquid cooling channels was investigated in [41]. It was found that in this channel configuration high flow rates limit the maximum temperature at the expense of pressure drop and temperature difference. A comparative study between serpentine and U-shaped cooling channels in [42] deduced that serpentine channels exhibit a better thermal performance. Similarly, the thermal performance of a square cooling channel is better than that of a circular channel, but it may result in a slight increase in the temperature non-uniformity, as shown in [43]. In addition, the aspect ratio of the cooling channel in a liquid cooling system may influence the thermal performance of a battery [44].

An oil-immersed battery cooling system could lower the battery temperature by 33% compared to natural convection [45]. This cooling system could also limit the temperature difference in the battery pack by keeping the temperature difference at 2.64 K at the end of a 2C discharge rate. Although a liquid cooling system may decrease the maximum temperature, it may increase the temperature difference in the battery pack. However, a new arrangement of fins on the cooling channels may reduce the maximum temperature by 27.63% and the temperature difference by 35.58% when compared with a pure paraffin cooled battery module [46].

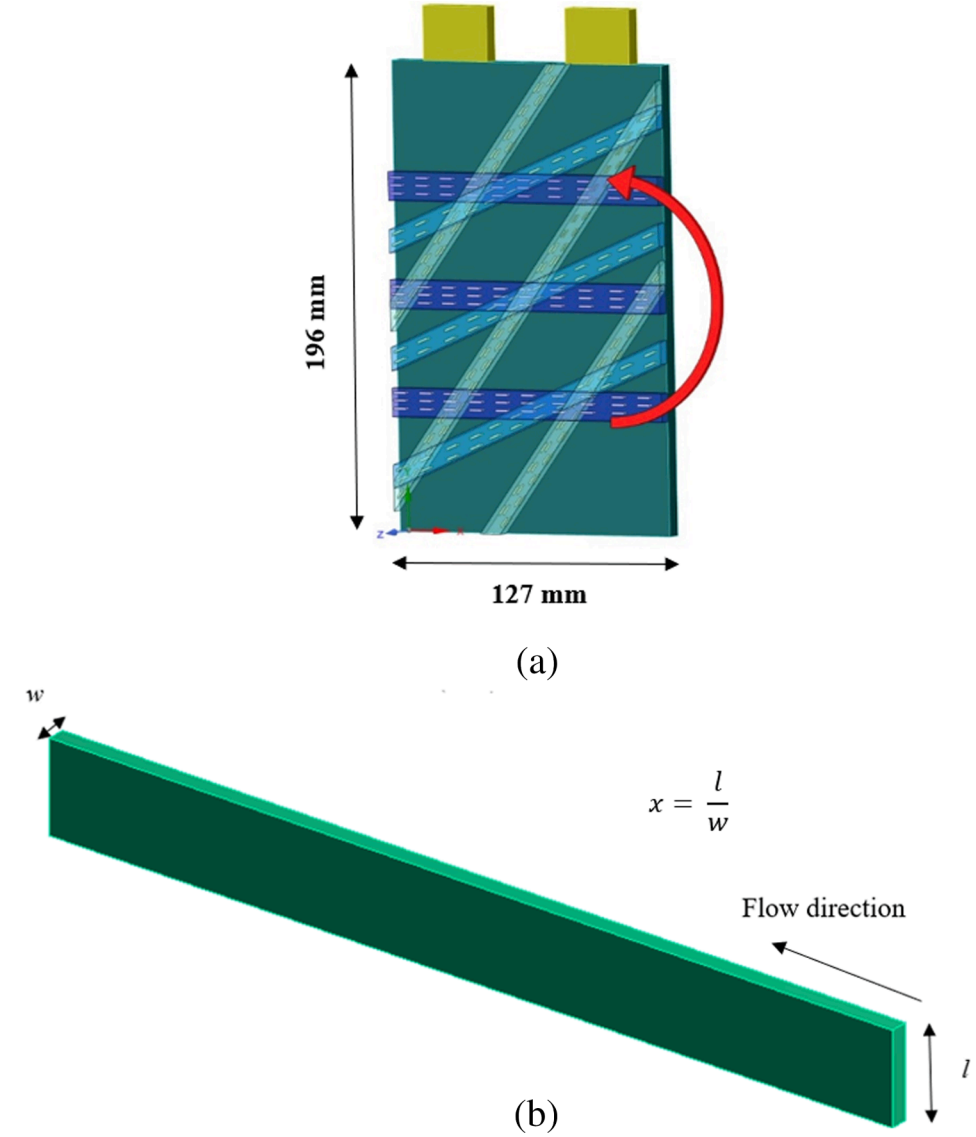

Fig. 3. (a) Depiction of mini-channels arranged at different inclination angles on the cell surface. (b) Single mini-channel.

Table 2
Material specifications.

Properties	P-tab	N-tab	Cell	Mini-channel fluid
Material	Aluminum	Copper	Active zone material	Water
Density (kg/m^3)	2719	8978	2092	998.2
Specific heat (J/kg-K)	871	381	678	4182
Thermal conductivity (W/m-K)	202	387.6	18.2	0.6

Table 3
Retrofitted battery structural details.

Components	Count	Height	Length	Width	Material
Cell	1	196 mm	127 mm	7 mm	Active zone material
P-tab	1	23 mm	30 mm	7 mm	P-tab material
N-tab	1	23 mm	30 mm	7 mm	N-tab material
Mini-channel	6 (2 × 3)	2 mm	Parameterized	Parameterized	Aluminum

An HCS using a composite PCM (CPCM) and liquid cooling was proposed in [47] for cooling a battery pack of 25 cylindrical cells at an ambient temperature of 313 K and a discharge rate of 5C. The CPCM featured 12% expanded graphite. The maximum battery pack temperature and the temperature difference at the end of the discharge rate were 318.24 K and 3.49 K, respectively, for a fluid inlet temperature of 313 K. It was observed also that an inlet temperature of less than 298 K perturbs the temperature difference in the battery pack. Direct liquid cooling of a 4S1P cylindrical battery pack (i.e., with 4 cells in series and 1 in parallel) was investigated in [48]. It was found that for all dielectric liquids the temperature rise could be limited to less than 5 K for a 2C discharge rate at a fluid mass flow rate of 0.05 kg/s. However, it was concluded in [49] that for fast charging Li-ion batteries, liquid cooling performs better than PCM-based cooling.

The publicly available literature hints toward liquid cooling systems as efficient options to reduce the maximum and average temperatures in a Li-ion battery. Channel parameters like fluid inlet velocity, contact-area between the channels and the battery surface, width and length of the channel, and fluid inlet temperature have been found to

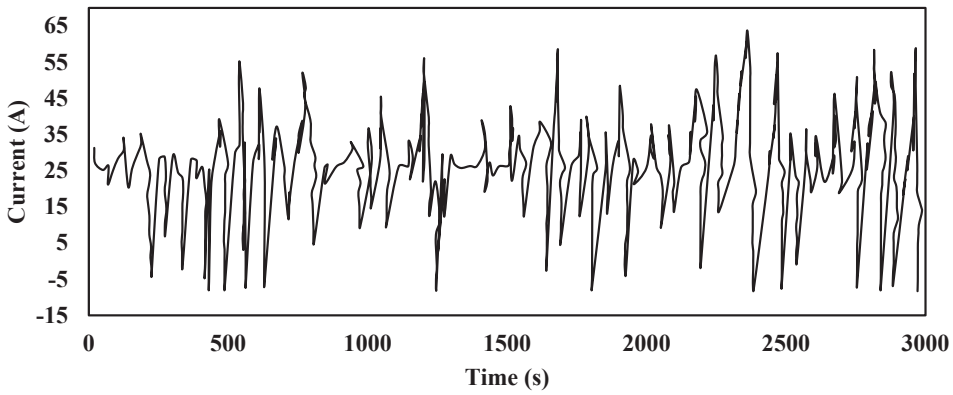

Fig. 4. Realistic driving cycle adopted in the present study [59]

Table 4
Key parameters of the hybrid bus.

Parameter	Value
Rated power (kW)	220
Battery/cell mass (kg)	0.07
Frontal area (m^2)	7.54
Aerodynamic drag coefficient	0.7
Rolling resistance coefficient	0.007
Wheel radius (m)	0.509
Final gear	4.7
Vehicle mass excluding hybrid energy storage system (ton)	14.5
Electric machine inertia (kg-m^2)	2.3
Inertia of final drive and wheels (kg-m^2)	41.8
Vehicular auxiliary power (kW)	7
Length of driving cycle (km)	16.55
Bus service period (year)	5

Table 5
Boundary conditions.

Boundary condition	Value
Heat transfer coefficient, h (W/m^2-K)	5
t_a (K)	313
$t_{initial}$ (K)	313

Table 6
NTGK Model parameters.

Coefficients used in U		Coefficients used in Y	
a_0	4.12	b_0	1168.59
a_1	–0.804	b_1	–8928
a_2	1.075	b_2	52504.6
a_3	–1.177	b_3	–136231
a_4	0	b_4	158531.7
a_5	0	b_5	–67578.5

Table 7
Mesh quality.

Properties	Mesh quality
Number of elements	1,760,662
Minimum orthogonal quality	0.61
Maximum orthogonal quality	1
Inflation option	smooth transition
Transition ratio	0.272
Growth rate	1.2

substantially impact the thermal performance of the battery pack. However, to the authors' best knowledge, limited information is available on how the different channel parameters correlate together toward a holistic mini-channel cold plate design that would, in turn, lead to an energy efficient cooling of the battery. To this end, this paper presents an optimized design of a liquid mini-channel cooling system for a prismatic Li-ion battery. A real-time driving cycle at an ambient temperature condition of 313 K has been considered. The influence of design parameters such as aspect ratio, inclination angle of the mini-channel, inlet fluid temperature, and parasitic power consumption have been studied through a broad parametric study. An experimentally validated model of the battery was simulated for 100 different designs of the mini-channel to enable an extensive parametric survey. The influence of each cooling channel parameter on the thermal performance of the battery was investigated individually and then in combination with all other parameters.

The goal of the research work was to design an effective and efficient EV battery cooling system where a balance between the cooling achieved in the retrofitted battery and the parasitic power consumption by the cooling system is achieved. While meeting this objective, the paper shows how the structural and flow parameters of a liquid cooling system should be prioritized in terms of their impact on the battery health and energy budget. For example, the rate of convective heat extraction from the heated battery to the coolant can be enhanced by increasing the temperature gradient between the battery and the coolant by having a colder fluid flow through the mini-channel. Alternatively, it can also be enhanced by increasing the convective heat transfer coefficient by, in turn, incrementing the mass flow rate of the coolant. To decide between these two possibilities, the cooling effectiveness and the energy economy of each option need to be assessed. Furthermore, a high coolant flow rate can be achieved by increasing the cross-sectional area of the mini-channel or by increasing the fluid velocity. Parasitic power consumption will rise when pumping a larger mass of coolant (resulting from a larger cross-section of the mini-channel) or when pumping a smaller mass of coolant at a higher velocity (to overcome a larger pressure drop in the mini-channel and achieve a high kinetic energy). This paper accounts for such competitive design aspects by holistically considering both heat transfer and energy economy to take adequate retrofitting decisions for a BTMS.

The widescale existence of hot climate in the two large continents Asia and Africa and the onset of frequent heat waves in Europe [50] and North America [51] indicate that if electric mobility options are promoted to substitute combustion-based vehicles, a large percentage of the EVs will have to endure hot ambient conditions. The present study offers an adequate cooling solution to ensure the safe functioning of power units of EVs, which is imperative for a large-scale transition toward electrification of transport.

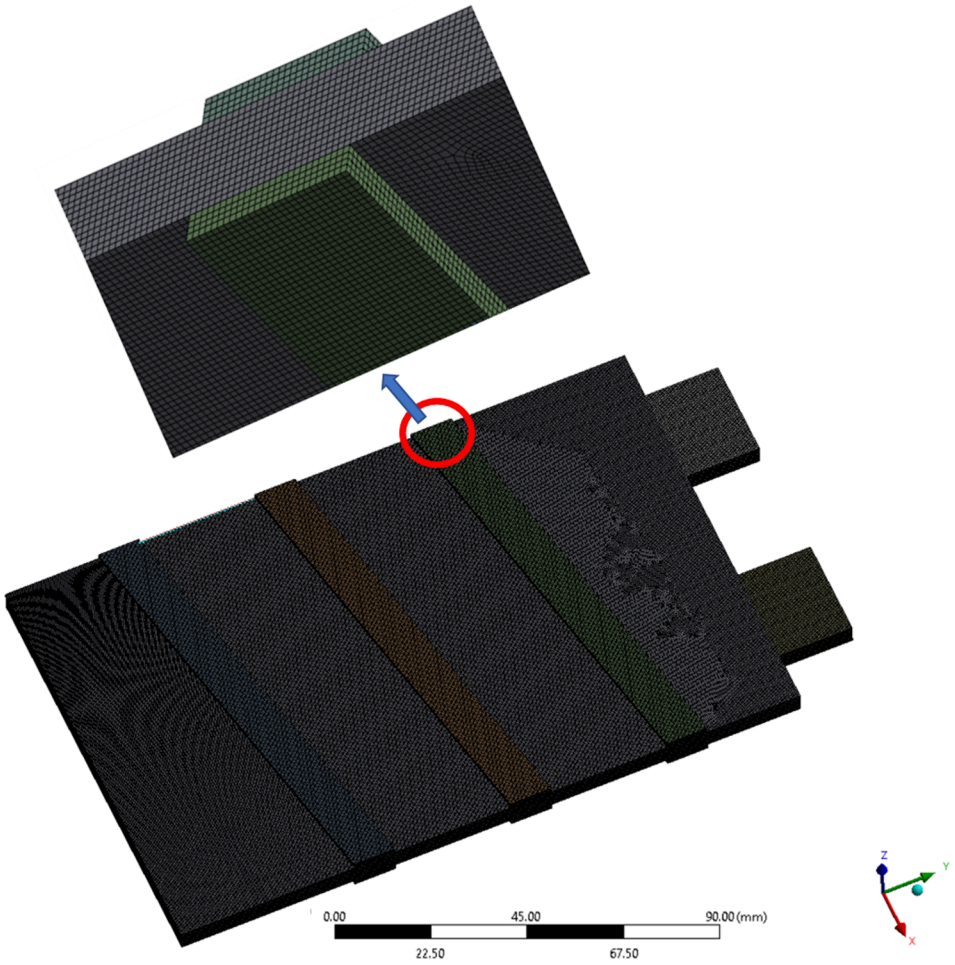

Fig. 5. Meshed image of the CFD model.

2. Materials and method

2.1. Research methodology

Given that this paper investigates the thermal management of a prismatic Li-ion battery in extreme ambient conditions, summer conditions in India with an ambient temperature of 313 K (40°C) were considered. As shown in Fig. 1, these conditions prevail across a vast extension of the Indian subcontinent.

The thermal performance of the retrofitted battery was analyzed under a realistic driving cycle. A detailed computational fluid dynamics (CFD) study and a subsequent parametric analysis were carried out to investigate the effect of mini-channel cooling on the battery. The evaluation criteria are based on the aspect ratio of the mini-channels, inclination angle of the mini-channels, fluid inlet temperature, fluid inlet velocity, mass flow rate, Reynolds number, pumping power, cooling work input (that is, cooling load), volume average temperature, and temperature difference. The parametric study entails a multi-criteria decision-making process to select a suitable design for the cooling retrofit.

2.2. Design of experiments

This section explains the design of experiments (DOE) framed to obtain the input variables for the present study. Four input parameters were considered: fluid inlet velocity, fluid inlet temperature, mini-channel inclination angle, and mini-channel aspect ratio. The lower and upper bounds of all 4 parameters are summarized in Table 1.

The LHS method, commonly used in the existing literature [53], was adopted to generate 100 design points within the lower and upper bounds of each input variable. The method randomly distributes the design points across the search space (i.e., the multi-dimensional space bounded by the maximum and minimum values of each parameter) and guarantees a variety of plausible design points while ensuring a stratified sampling. Each input variable can attain any value within its range. Furthermore, the LHS method has a better distribution of data with fewer design points in comparison to standard random sampling, where a higher number of samples is required to obtain accurate output variables [54,55]. Another advantage of this method is its less expensive numerical computations [56].

The LHS method generates DOEs of size 'N' from 'y' variables; that is, $y_1, y_2, y_3, \ldots, y_n$. The range of each variable is then partitioned into non-repeating intervals with an equal probability of $1/N$. The values are randomly selected from the intervals as per the probability density. The 'N' values, which are randomly selected for y_1, are then paired randomly with 'N' values of y_2, and so on. Thus, the set of $N \times n$ tuples constitutes the LHS distribution of randomly sampled independent variables. $(N!)^{n-1}$ possible interval combinations exist for given values of N and n [57].

In this paper, the ANSYS Design Explorer was used to generate the LHS-based DOE. Fig. 2 shows the sample selection and distribution of the 100 design points, which are randomly distributed within the set range.

2.3. Criteria for evaluation of the thermal performance of the BTMS

The following parameters were considered to investigate the thermal

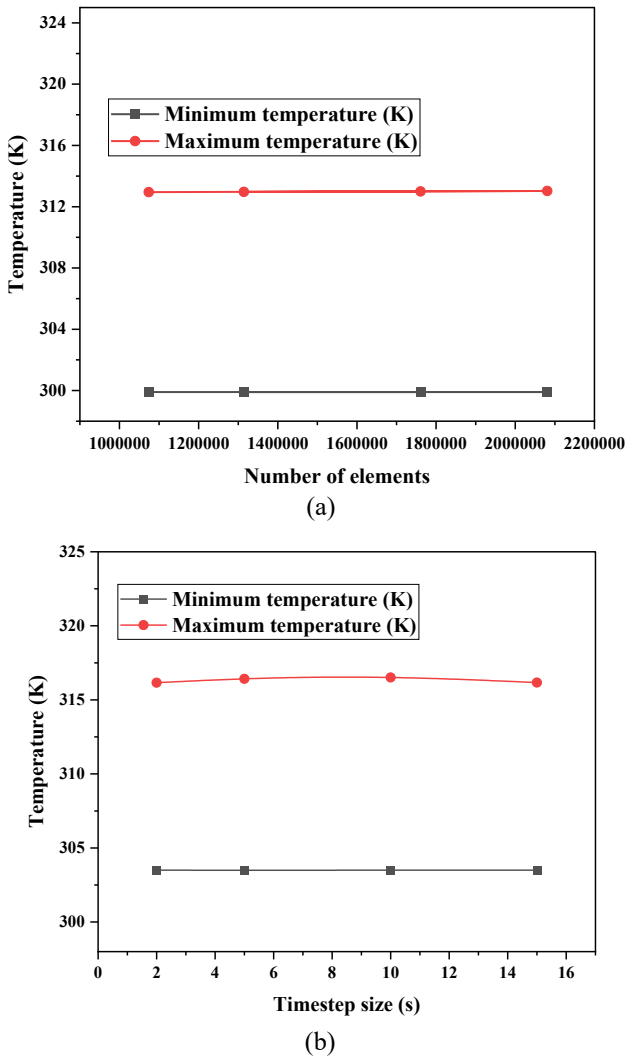

Fig. 6. (a) Mesh independence study. (b) Timestep size independence study.

performance of the mini-channel cooling technology:

i. Volume average temperature: This output parameter is the volume average temperature of the cell, P-tab, and N-tab bodies.

ii. Temperature difference: This output parameter is the difference between the minimum and maximum temperatures on the cell surface.

iii. Aspect ratio (x): It is the ratio of the width (l) to the height (or thickness) (w) of the mini-channel (shown in Fig. 3). The height or thickness is fixed at 2 mm and the width is parametrized.

iv. Fluid inlet velocity (v): This is the velocity at which the liquid coolant enters the mini-channel.

v. Mass flow rate (m): This is the mass flow rate of liquid coolant through the mini-channels.

vi. Reynolds number (Re): This is a dimensionless number calculated for each case and its effect is observed on the thermal performance of the Li-ion battery. It is calculated with

$$\mathrm{Re} = \frac{\rho v D_h}{\mu} \tag{1}$$

$$D_h = \frac{4(w \times l)}{2(w + l)} \tag{2}$$

where Re denotes the Reynolds number, ρ is the density of the fluid, v is the velocity of the fluid at the inlet, D_h is the hydraulic diameter of the mini-channel, μ is the dynamic viscosity of the fluid, w is the mini-channel's height or thickness, and l is the mini-channel's width.

vii. Inclination angle (i): This is the angle between the longitudinal axes of the mini-channels with respect to the horizontal base of the battery.

viii. Fluid inlet temperature (t_i): This is the temperature at which liquid coolant is supplied at the mini-channel inlet.

ix. Pumping power (W_P): This is the power required to pump coolant through the mini-channels. It is calculated as [58]

$$W_P = \Delta P \times Q \tag{3}$$

$$\Delta P = \frac{fL\rho v^2}{2D_h} \tag{4}$$

where the friction factor (f) is given by:

$$f = \frac{24}{\mathrm{Re}} \times \left(1 - \frac{1.3553}{x} + \frac{1.7467}{x^2} - \frac{1.7012}{x^3} + \frac{0.9564}{x^4} - \frac{0.2537}{x^5}\right) \tag{5}$$

x. Work input or cooling power required (W_c): This is the work required to supply coolant at a desired temperature at the inlet of the mini-channel. It is calculated using:

$$W_c = \frac{q}{\mathrm{COP}} \tag{6}$$

$$q = mC_P(t_a - t_i) \tag{7}$$

where q is the cooling load, COP is the coefficient of performance (COP), m is the mass flow rate of coolant, C_P is the specific heat of coolant, and t_a is the ambient temperature. The work input is calculated by assuming that the refrigeration cycle of the air conditioning system has a constant COP of 2 in all operating conditions [59].

2.4. Multi-criteria decision-making for optimal design selection

Based on the parameters defined in Section 2.3, the performance of the BTMS was evaluated for all the 100 design cases considered. The suitability of a particular retrofit configuration is judged based on the average temperature of the volume, the power consumption by the BTMS (cooling power) and the temperature difference. A suitable BTMS is expected to minimize all the 3 parameters. Since different design cases achieve this objective in different levels for the judging criteria, the multi-criteria decision-making algorithm called Technique for Order Preference by Similarity to an Ideal Solution (TOPSIS) was adopted to select the most suitable case.

An entropy-based TOPSIS method was implemented to prioritize design cases (according to the 3 judging criteria) without involving any human-induced bias in the selection of the best case [60,61]. A more detailed description about the TOPSIS method and explanations for its different stages of formulation can be found in [62]. The mathematical equations to implement the entropy-based TOPSIS selection are shown next (in the sequence of computation for the sake of brevity).

Scoring matrix:

$$D = \begin{bmatrix} x_{11} & \cdots & x_{1j} & \cdots & x_{1n} \\ \vdots & & \vdots & & \vdots \\ x_{i1} & \cdots & x_{ij} & \cdots & x_{in} \\ \vdots & & \vdots & & \vdots \\ x_{m1} & \cdots & x_{mj} & \cdots & x_{mn} \end{bmatrix} \tag{8}$$

where D is a matrix of scores (x_{ij}) belonging to "m" design options under "n" different criteria to assess the suitability for each design.

Standardized matrix:

$$r_{ij} = \frac{x_{ij}}{\sqrt{\sum_{i=1}^{m} x_{ij}^2}}; i = 1, 2, \ldots, m; j = 1, 2, \ldots, n \tag{9}$$

where r_{ij} represents the standardized scores.

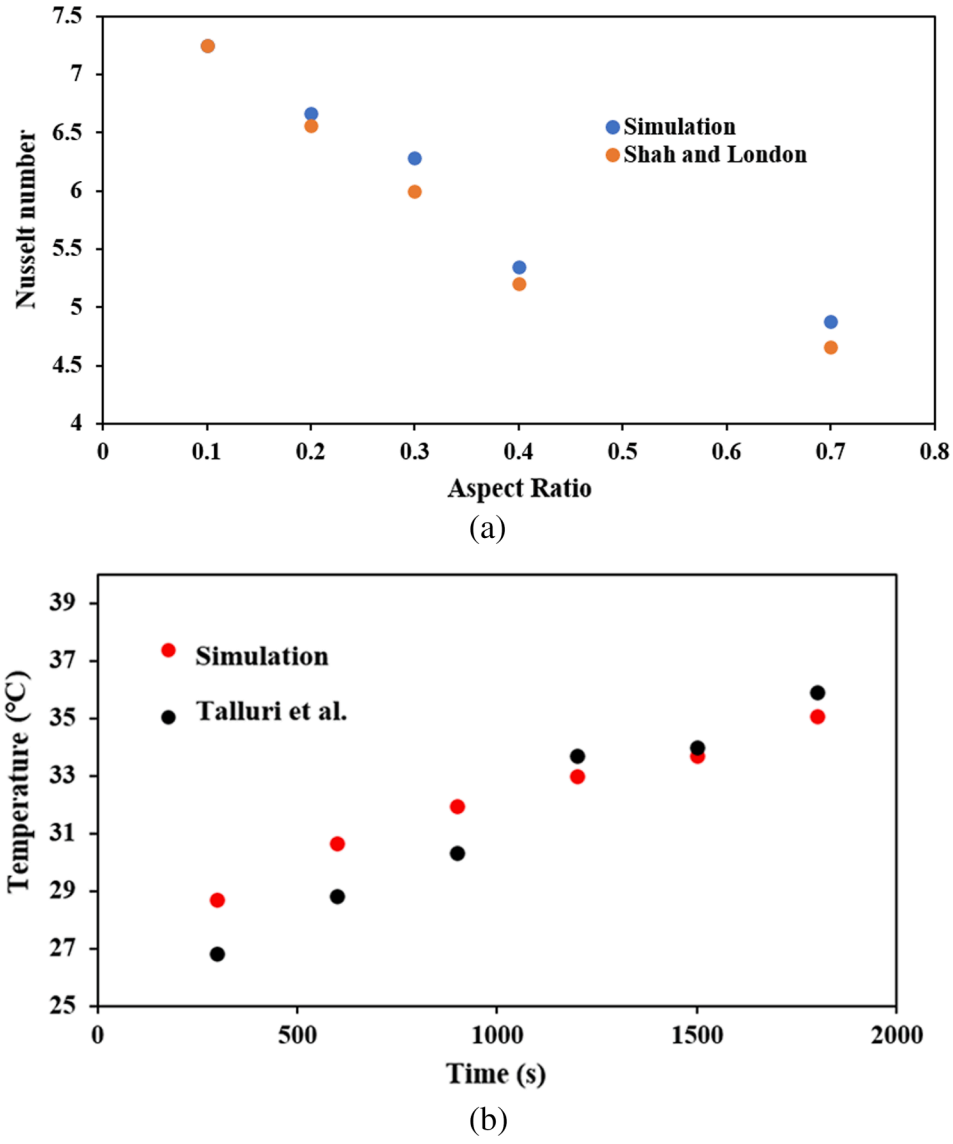

Fig. 7. Validation: (a) Ref. [69] (flow through mini-channel). (b) Ref. [70] (battery model).

Proportional calculation:

$$p_{ij} = \frac{x_{ij}}{\sum_{i=1}^{m} x_{ij}}; i = 1, 2, \ldots, m; j = 1, 2, \ldots, n \tag{10}$$

where p_{ij} represents the proportion for every score in D.

Entropy calculation:

$$e_j = -\frac{1}{\ln(m)} \sum_{i=1}^{m} p_{ij} \times \ln(p_{ij}) \tag{11}$$

where e_j represents the entropy for criterion j.

Entropy weight calculation:

$$w_j = \frac{(1 - e_j)}{\sum_{j=1}^{n} (1 - e_j)} \tag{12}$$

where w_j denotes the weight for criterion j computed by the entropy method.

Weighted matrix calculation:

$$v_{ij} = w_j r_{ij}; i = 1, 2, \ldots, m; j = 1, 2, \ldots, n \tag{13}$$

where v_{ij} represents the weighted score.

Ideal solution:

$$A^{+} = \left\{ \left(\max_i x_{ij} | j \in J_1 \right), \left(\min_i v_{ij} | j \in J_2 \right) | i = 1, 2, \ldots, m \right\} = v_1^{+}, v_2^{+}, \ldots, v_n^{+} \tag{14}$$

where A^+ is the ideal solution that contains the best values for every criterion (v_1^+, v_1^+..., v_n^+).

Anti-ideal solution:

$$A^{-} = \left\{ \left(\min_i x_{ij} | j \in J_1 \right), \left(\max_i v_{ij} | j \in J_2 \right) | i = 1, 2, \ldots, m \right\} = v_1^{-}, v_2^{-}, \ldots, v_n^{-} \tag{15}$$

where A^- is the anti-ideal solution that contains the worst values for every criterion (v_1^-, v_1^-..., v_n^-).

In (14) and (15), J_1 represents the most suitable value of the j^{th} criterion when it is profitable. Conversely, J_2 stands for when it is unprofitable.

Euclidian distance from the ideal solution (S_i^+):

$$S_i^{+} = \sqrt{\sum_{j=1}^{n} \left(v_{ij} - v_j^{+} \right)^2}; i = 1, 2, \ldots, m \tag{16}$$

Euclidian distance from the anti-ideal solution (S_i^-):

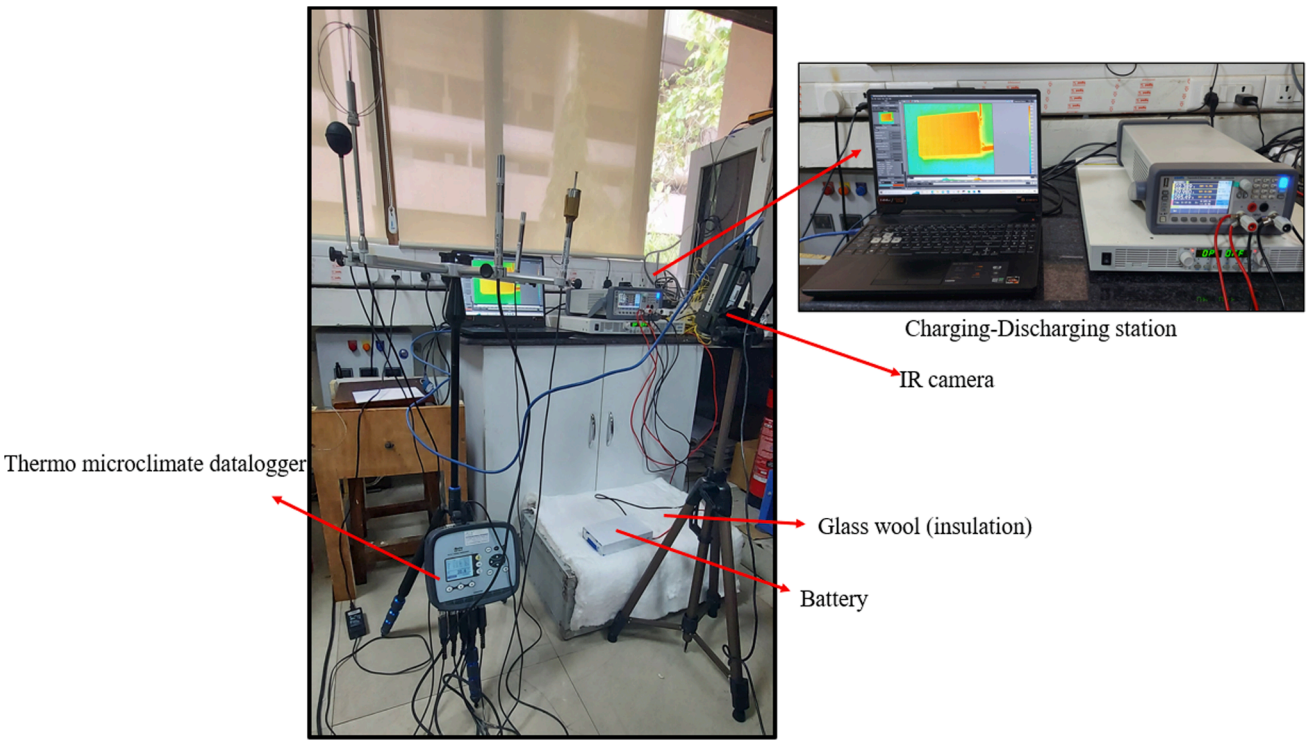

Fig. 8. Experimental setup.

$$S_i^- = \sqrt{\sum_{j=1}^{n}\left(v_{ij} - v_j^-\right)^2}; i = 1, 2, \ldots, m \tag{17}$$

Closeness degree calculation (C_i^+):

$$C_i^+ = \frac{S_i^+}{S_i^+ + S_i^-}; i = 1, 2, \ldots, m \tag{18}$$

Larger values of C_i^+ indicate a better suitability of a particular design (and vice versa). Therefore, the best design is chosen as the one that yields the largest value of C_i^+.

2.5. Numerical model of the BTMS

A battery is an electrochemical unit which consists of electrodes, a separator, and an electrolyte. There are two main considerations toward developing a holistic battery model: the simulation should not be time-consuming and costly, and it should be accurate. For instance, battery models based on electrochemical reactions are accurate but time-consuming.

The 14.6 Ah prismatic battery investigated in [63], with dimensions 127 mm × 196 mm × 7 mm, was here considered as it is widely used in EVs. The material specifications of the numerical model are provided in Table 2 [64]. ANSYS Fluent 2020 R1 was used for the simulations, which were conducted using the high-performance computing (HPC) facility of IIT-Delhi.

The battery tabs are considered as passive zones and the cell as an active zone because all the electrochemical reactions occur inside the cell. Fig. 3 shows the geometry of the Li-ion cell. The battery is retrofitted with 6 mini-channels (3 each on the X-Y plane surfaces of the cell). As mentioned previously in Section 2.3, the height of the mini-channels was fixed at 2 mm and the width was parameterized. The direction of the coolant flow is in a counter-flow pattern for the two battery surfaces. This pattern of the coolant, in this case water, helps in assessing the localized heating at the outlet. This also prevents hotspots in the vicinity. The structural details of the retrofitted battery are given in Table 3.

The driving cycle (current profile) is shown in Fig. 4. This was adopted from the simulation of a hybrid-electric bus, where the total distance covered and the time taken for the analysis period were 16.55 km and 3000 s respectively [59]. The bus is powered by an electric machine with a power rating of 220 kW and a 100 kW fuel cell system based on an unpressurized proton-exchange-membrane. Key parameters of the bus are given in Table 4 [65]. The average heat generation in the cyclic load corresponds to that of a 4.25C constant-current (C–C) rate. The discharge current is positive in the cyclic loading.

The assumptions considered in the CFD modelling in this study are summarized below:

i. Free convective heat transfer was considered from the surfaces of the retrofitted battery pack.
ii. Constant specific heat and density values were considered for the coolant.
iii. A laminar viscous model was considered in the simulation.

The taken boundary conditions are listed in Table 5.

The complex physics of the Li-ion battery were captured by using the dual potential multi-scale multi-dimensional model (MSMD) approach available in ANSYS Fluent. The anode-separator-cathode sandwich layers hold the overall physics occurring inside the battery. The electrical and thermal fields are solved in the CFD domain using the MSMD approach with the following equations:

$$\frac{\partial \rho C_P T}{\partial t} - \nabla\cdot(k\nabla T) = \dot{q} \tag{19}$$

$$\nabla\cdot(\sigma_+\nabla\varphi_+) = -J \tag{20}$$

$$\nabla\cdot(\sigma_-\nabla\varphi_-) = J \tag{21}$$

where

σ_+ is the effective electrical conductivity of the positive electrode,
σ_- is the effective electrical conductivity of the negative electrode,
φ_+ is the phase potential for the positive electrode,
φ_- is the phase potential for the negative electrode,

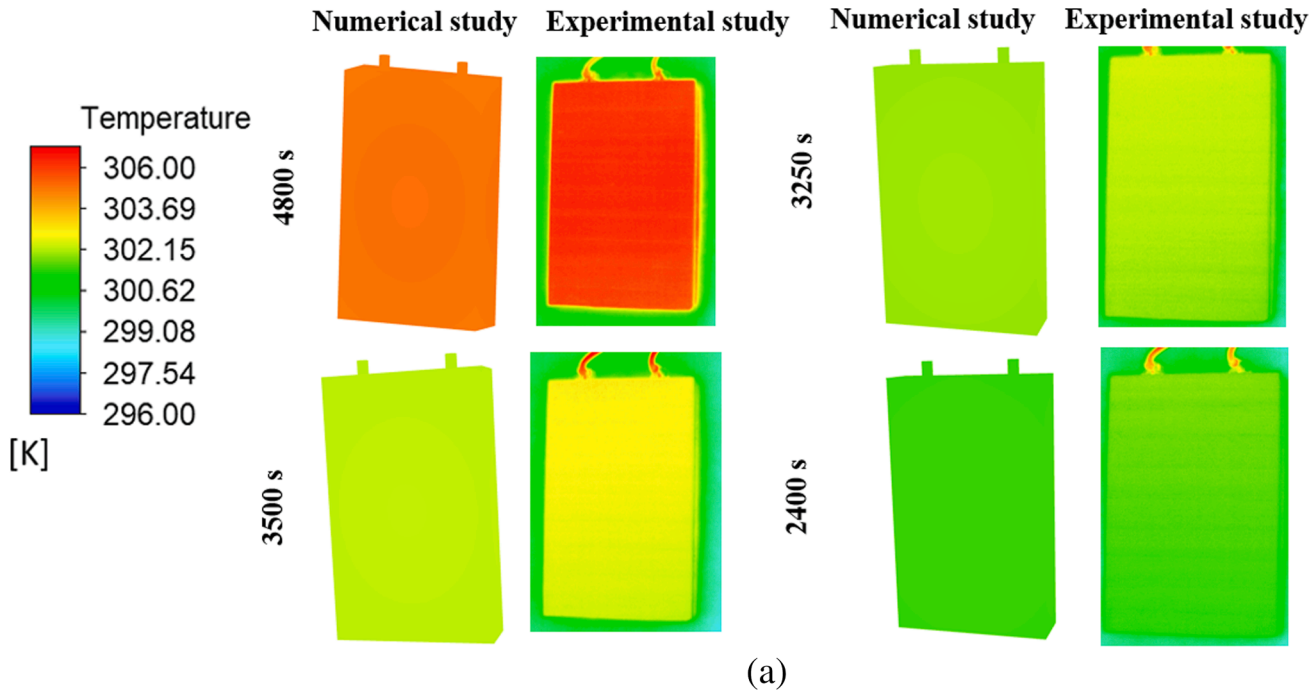

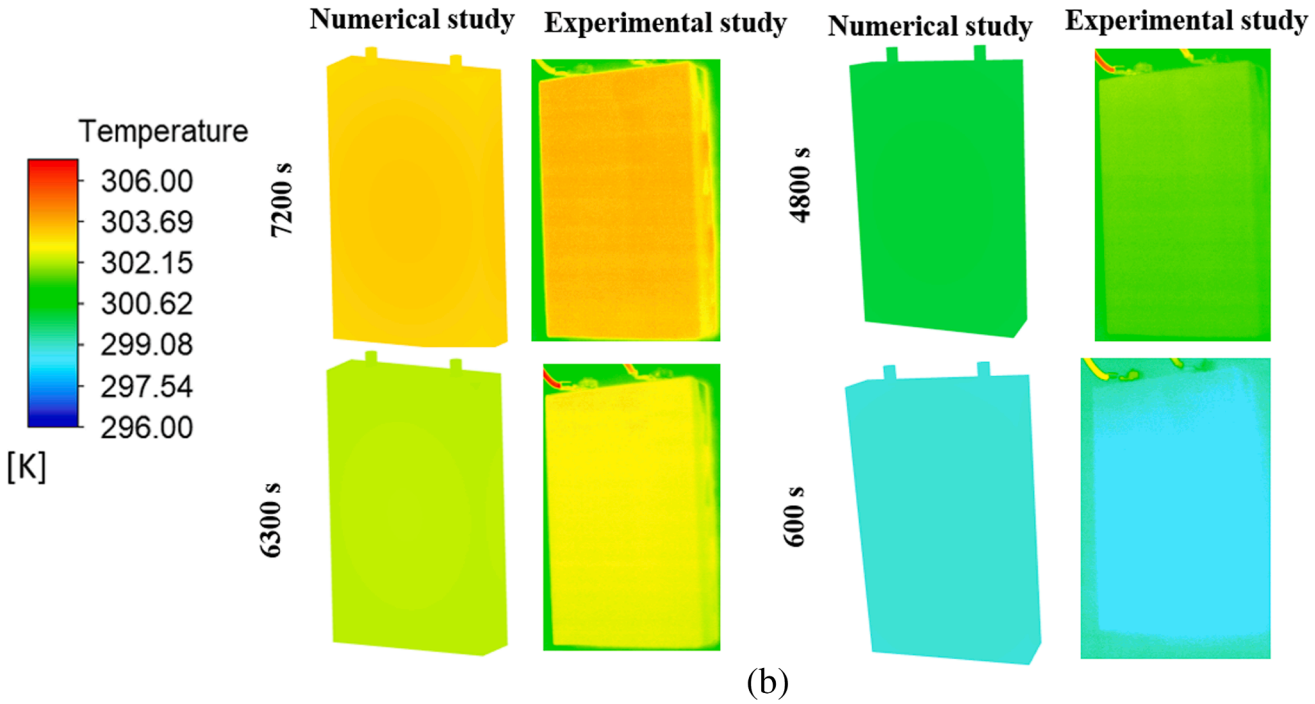

Fig. 9. Comparison between the experimental and numerical solutions: (a) 0.8C; (b) 0.5C.

J is the volumetric transfer for current density, and
$\dot{q}$ is the heat generation rate during battery operation.

The Newman, Tiedemann, Gu, and Kim (NTGK) semi-empirical electrochemical model was selected to conduct the battery simulations. The rationale behind this model choice is that it successfully predicts the coupled thermochemical characteristics of a battery cell, with an average deviation between experimental and numerical results reported to be less than 1 K [66]. In an NTGK model, the volumetric transfer for current density (J) in terms of phase potential (φ) is given as:

$$J = aY[U - (\varphi_+ - \varphi_-)] \tag{22}$$

where a is the specific area of the electrode sandwich sheet. Y and U are model parameters, obtained through a curve fitting process of voltage-current response curves of a reference battery (with a capacity of 32.77 Ah), and are functions of the depth of discharge (DOD), with

$$Y = \left(\sum_{n=0}^{5} a_n \mathrm{DOD}^n\right) \mathrm{e}^{-C_1\left(\frac{1}{T}-\frac{1}{T_{ref}}\right)} \tag{23}$$

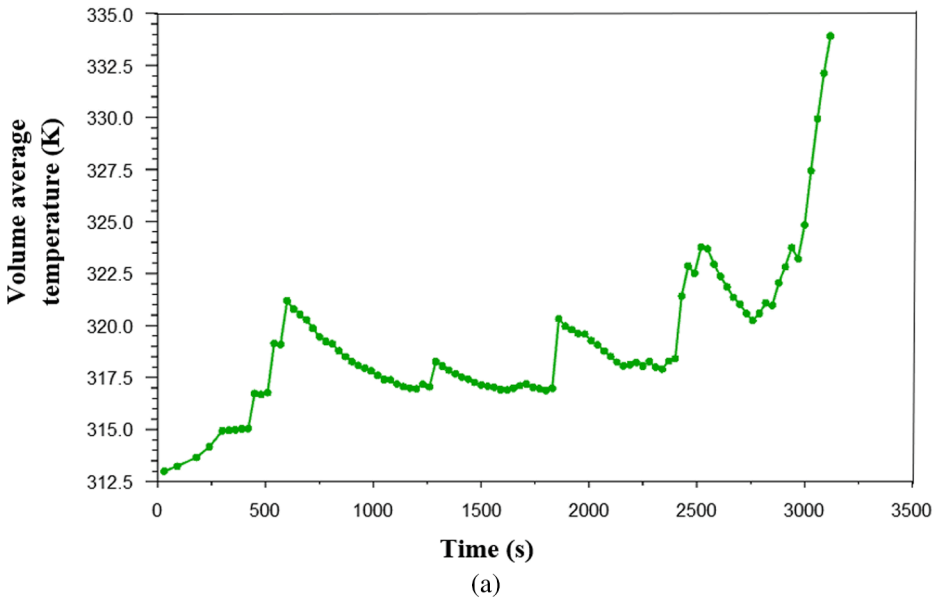

(a)

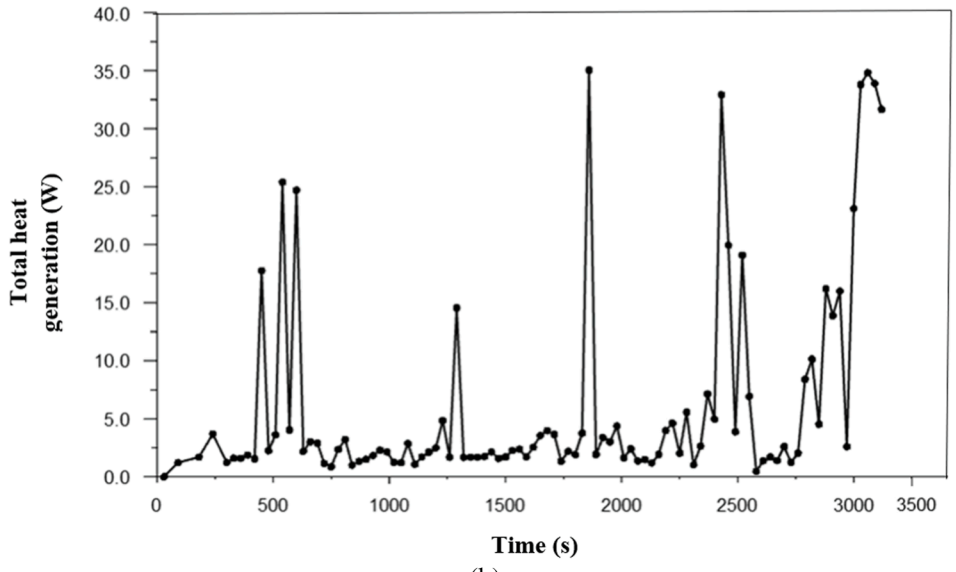

(b)

Fig. 10. Plots for: (a) volume average temperature with time; (b) total heat generation with time.

$$U = \left(\sum_{n=0}^{3} b_n \mathrm{DOD}^n\right) - C_2\left(T - T_{ref}\right) \tag{24}$$

$$\mathrm{DOD} = \frac{V}{3600 Q_{Ah}}\left(\int_0^t J dt\right) \tag{25}$$

where V denotes the volume of the battery and Q_{Ah} stands for its capacity in Ampere-hours. Constant temperature corrections are given as $C_1 = 1800$ and $C_2 = -0.00095$. The details of the NTGK model parameters are provided in Table 6.

Heat is generated because of the reversible and irreversible heat sources in the operation of the battery. Joule heating, electrochemical reaction heating, and entropic heating are the main causes of heat generation inside the battery. The heat source term is given as:

$$\dot{q} = \sigma_+ \nabla^2 \varphi_+ + \sigma_- \nabla^2 \varphi_- + J\left[U - (\varphi_+ - \varphi_-) - T\frac{dU}{dT}\right] \tag{26}$$

The study includes liquid cooling. The governing equations of the process are defined by the fundamental equations of continuity, momentum, and energy, namely

$$\nabla \cdot \vec{V} = 0 \tag{27}$$

$$\rho \frac{\partial \vec{V}}{\partial t} + \rho\left(\vec{V} \cdot \nabla\right)\vec{V} = -\nabla P + \mu \nabla^2 \vec{V} + \rho \vec{g}(T - T_a) + \vec{S} \tag{28}$$

$$\rho \frac{\partial (H)}{\partial x} + \rho \nabla \cdot (Vh) = k \nabla^2 T + S_h \tag{29}$$

The need for a large computational time for the CFD simulations with the NTGK model and the complexity of the solution were relieved by adopting a reduced order method (ROM). The ROM reduces the partial differential equations describing the system to ordinary differential equations and linearizes the non-linear equations. The ROM runs orders of magnitude faster than the original CFD model [67]. For example, in [68], a CFD model for an automotive battery module with 28 cells was simulated with and without ROM and the results were compared. The percentage error between the results for 10, 20, 30, and 40 s of simulation time were 1.4%, 0.7%, 0.49%, and 0.59%, respectively. It was also observed that the ROM reduced the simulation time drastically. The

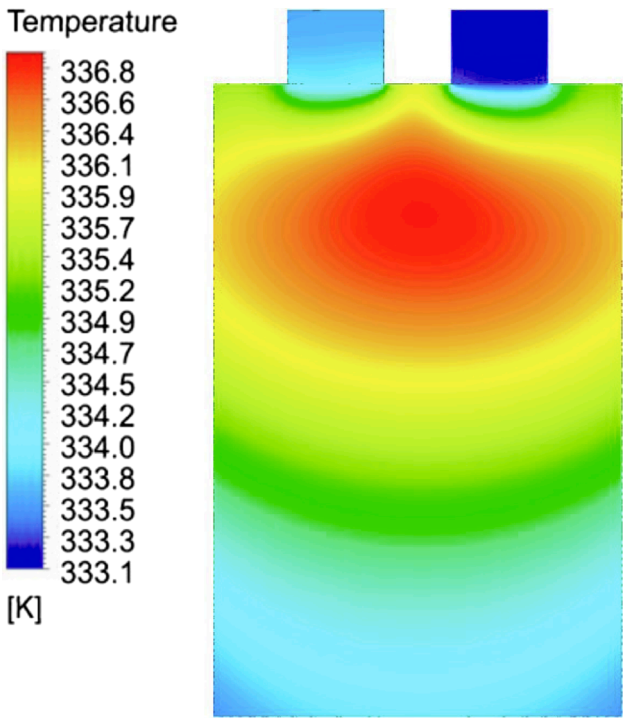

Fig. 11. Temperature contours for the battery without a BTMS.

CFD run took approximately 20 hours of simulation time on six CPUs, whereas with the ROM the simulation time was in the order of seconds using a single CPU.

3. Model stability and validity assessment

The numerical model presented in Section 2 is examined in this section through standard tests to ascertain its validity.

3.1. Mesh and timestep size independence check

To verify the stability of the model, this section explains the mesh details and the solution independence check performed on mesh and timestep size. Table 7 lists the properties of the mesh. A structured hexahedral mesh was used to ensure high quality. This is shown in Fig. 5, and it has 1,760,662 elements.

Four different grid sizes were tested to assess mesh independence, namely 1,074,132, 1,314,216, 1,760,662 (i.e., the mesh with properties provided in Table 7), and 2,080,785 elements. In these tests, the fluid inlet velocity, inlet temperature, aspect ratio, and inclination angle were set as 0.33 m/s, 299.9 K, 6.3, and 11.3° respectively. As shown in Fig. 6 (a), the small change in minimum and maximum temperatures confirms the model stability and the grid independence of the numerical solution. The transient response of the model was recorded by taking four different timestep sizes of 2 s, 5 s, 10 s, and 15 s, with results shown in Fig. 6(b). The minor changes in the temperature values demonstrate the timestep size independence of the solution for the present battery model.

3.2. Model validation

The approach on laminar flow in rectangular ducts followed in [69] was used to validate the mini-channel cooling system design for this study. The Nusselt number (Nu) for laminar flow is defined as

$$\mathrm{Nu} = \frac{hD_h}{K_w} \tag{30}$$

The variation of Nu with the aspect ratio was recorded for different values of aspect ratio and compared with the results available in [69]. Fig. 7(a) shows the results of this comparison. It is observed that there is good agreement between the sets of results.

The experimental study reported in [70] was used to validate the NTGK battery model used in this paper. In the study, the prismatic Li-ion battery was discharged at a 2C rate at an ambient condition of 299.1 K. Fig. 7(b) shows the results from the validation. The small deviation between the simulation results and the experimental data reported in [70] demonstrates the validity of the battery model.

3.3. Experimental validation of the NTGK model

To justify the suitability of the NTGK battery model, in addition to the comparison with the numerical results in [69] and the experimental results in [70], an experimental validation of the model was also carried out. However, for such a verification exercise it was not possible to use the commercial battery described in Section 2.5. Instead, a 50 Ah prismatic Li-ion battery was employed for the experiment as this was available to undertake research activities. This battery has a larger capacity than the 14.6 Ah unit described in Section 2.5, but it enabled it to maintain a safe operation during the experiments upon the occurrence of over-charging or over-discharging incidents.

The implementation of the NTGK model was done in a similar manner for this 50 Ah battery as was done for the 14.6 Ah battery. Fig. 8 shows the experimental setup consisting of the battery (50 Ah), a charging-discharging station, an infrared (IR) imaging camera, and a PT-100 temperature sensor. The battery was placed horizontally on a glass wool sheet. An FLIR A325sc IR camera was used to obtain thermal images of the battery at discharge rates of 0.8C (40 A) and 0.5C (25 A). The camera has an uncooled Vanadium oxide microbolometer detector that produces thermal images of 320 × 240 pixels with a reading accuracy of ±2 K or ±2%. The standard temperature range of the camera is 253 K to 393 K.

The thermal images retrieved with the experiment were compared with the contours obtained through the numerical study (implementing the NTGK model on the 50 Ah prismatic battery), with results of this comparison shown in Fig. 9. The close agreement between experimental and numerical results ratifies the validity of the NTGK battery model used.

4. Results and discussion

4.1. Battery without BTMS under a real driving cycle

As the baseline case, the realistic driving cycle presented in Fig. 4 was first imposed on the Li-ion battery without any BTMS supporting its operation. The battery's volume average temperature variation over the driving cycle is shown in Fig. 10(a). The maximum temperature at the end of the driving cycle was 336.95 K. The variation of heat generated in the battery is shown in Fig. 10(b), with a maximum heat generated of 35 W. Fig. 11 shows the temperature contour of the battery. The DOD at the end of the driving cycle was 0.4. This case was then analyzed against the retrofitted battery with coolant mini-channels, with results discussed in the subsequent sections.

4.2. Effect of fluid inlet temperature on a retrofitted battery

The effect of the fluid inlet temperature on the volume average temperature and the temperature difference in the battery is shown in Fig. 12(a). The temperature difference increases with a decrease in fluid inlet temperature, whereas the volume average temperature follows the opposite trend. The minimum and maximum temperature difference values (0.31 K and 13.02 K) occurred at fluid inlet temperatures of 310.2 K and 298.2 K, respectively.

The minimum volume average temperature value was 301.1 K for a fluid inlet temperature of 298.1 K. Also, the maximum volume average temperature value of 315.9 K occurred for a fluid inlet temperature of 310.5 K. It is to be noted that these average temperature extremities

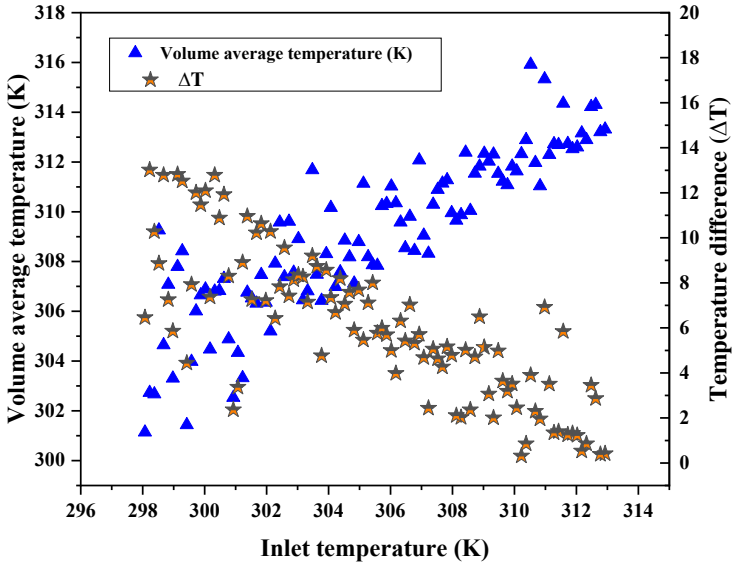

(a)

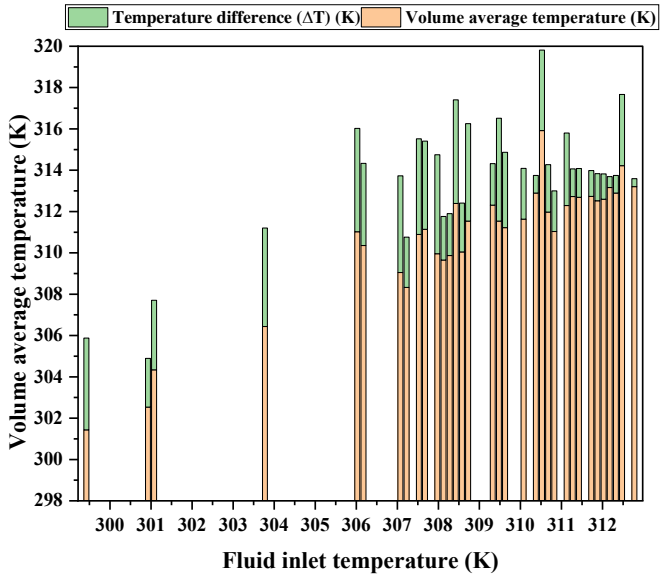

(b)

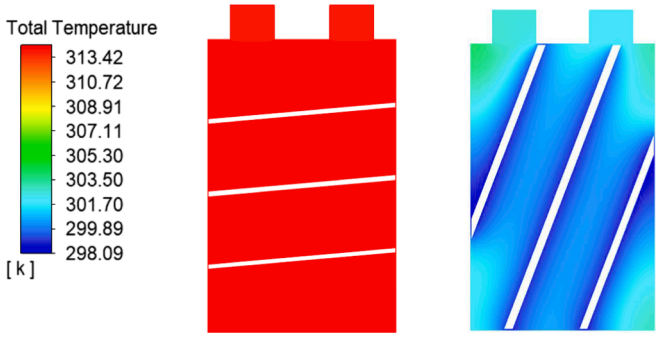

(c)

Fig. 12. (a) Plot showing the effect of fluid inlet temperature on volume average temperature and temperature difference in the cell. (b) Plot showing DOEs with a temperature difference less than 5 K. (c) Comparative temperature contours for fluid inlet temperature 312.9 K ($i = 5°$) and 298.1 K ($i = 68.9°$).

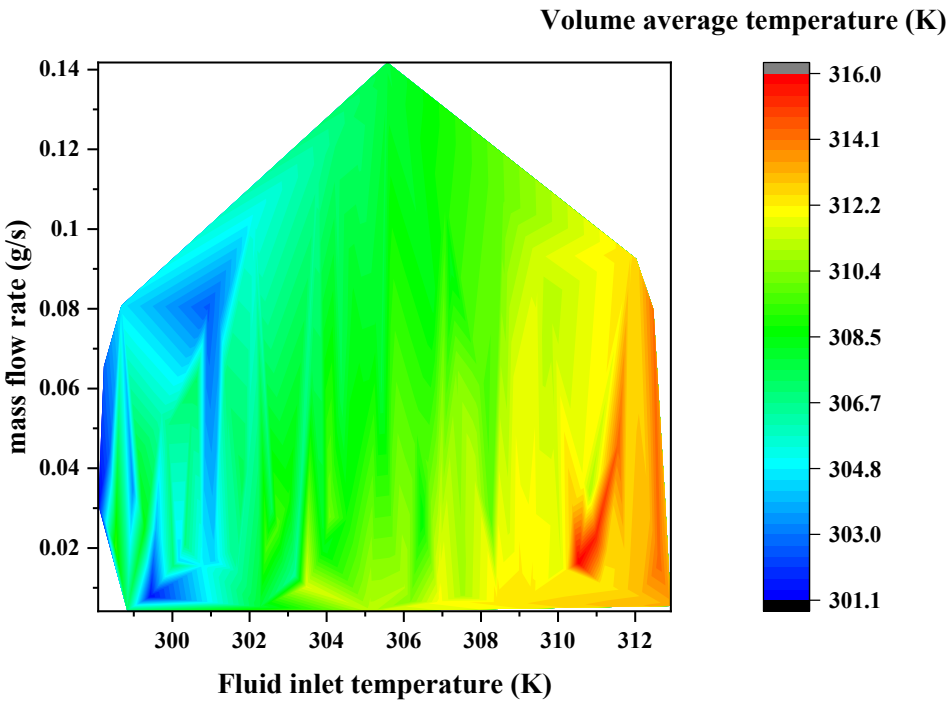

Fig. 13. Effect of mass flow rate and fluid inlet temperature on volume average temperature.

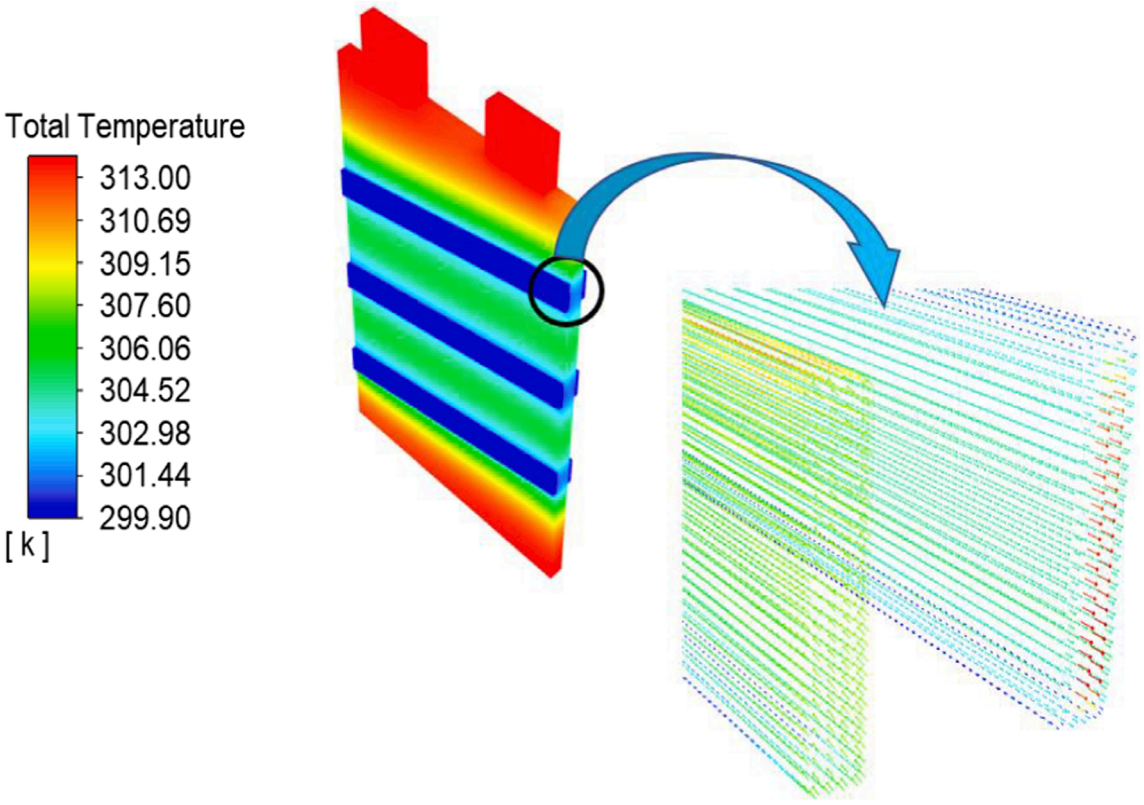

Fig. 14. Counter-flow depiction in the mini-channels.

have different DOEs (input parameters). Except for a few exceptional cases, a decrease in fluid inlet temperature increased the temperature difference in the battery. This is because although intense local cooling induced by mini-channels can substantially cool down certain regions of the battery, the regions distant from the mini-channels create a high temperature gradient across the battery. Therefore, a high degree of cooling provided through very cold fluid may be less desirable due to the high temperature differences.

The temperature difference within the cells of the battery pack must be less than 5 K to avoid the uneven temperature distribution that helps preventing the adverse effects of thermal perturbances [8]. The DOEs which yielded a temperature difference below this value are shown in

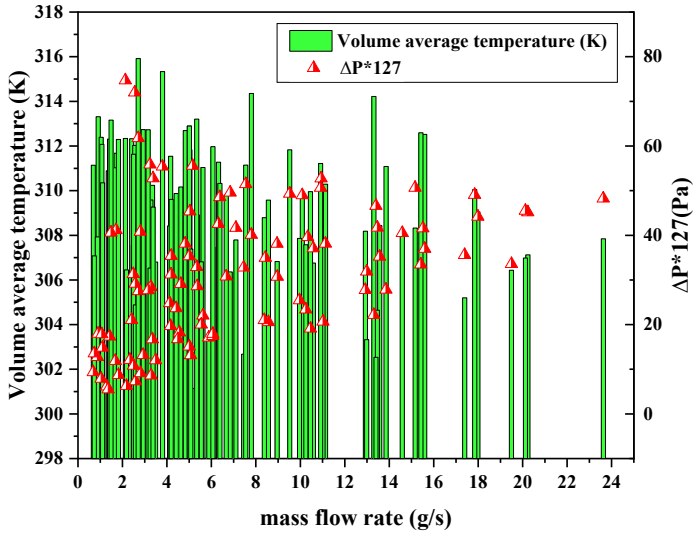

(a)

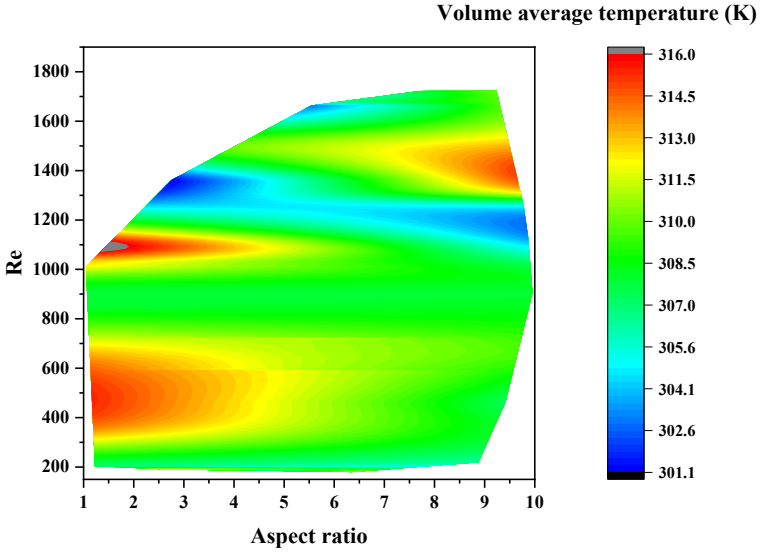

(b)

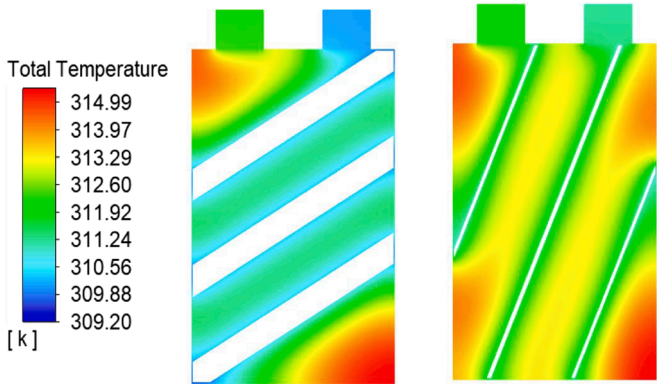

(c)

Fig. 15. (a) Plot showing the effects of mass flow rate on pressure drop and volume average temperature. (b) Graphical plot showing the effects of the aspect ratio and Re on the volume average temperature. (c) Comparative temperature contours for mini-channel aspect ratios of 8.1 ($i = 31.1^\circ$ and 1.1 ($i = 67.1^\circ$).

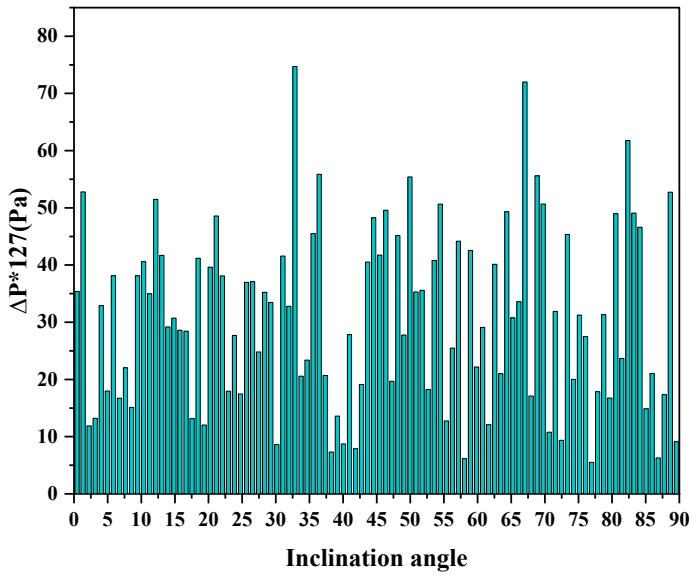

(a)

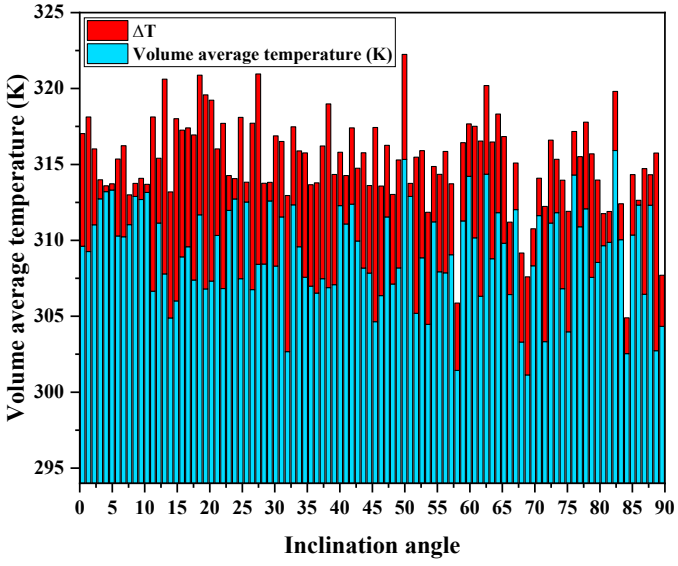

(b)

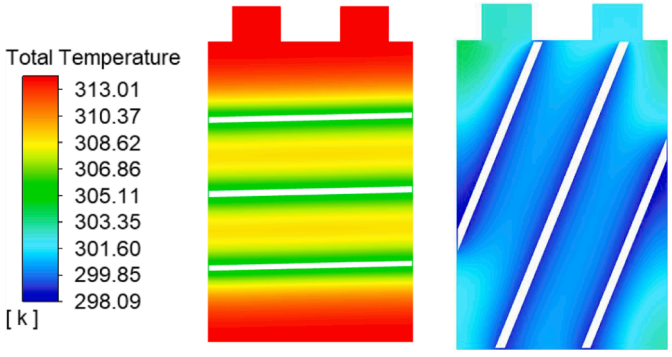

(c)

Fig. 16. (a) Plot showing the effect of inclination angle on the pressure drop. (b) Plot showing the effects of inclination angle on volume average temperature and temperature difference. (c) Comparative temperature contours for inclination angles of 1.4° and 68.9° for a fluid inlet temperature of 298 K.

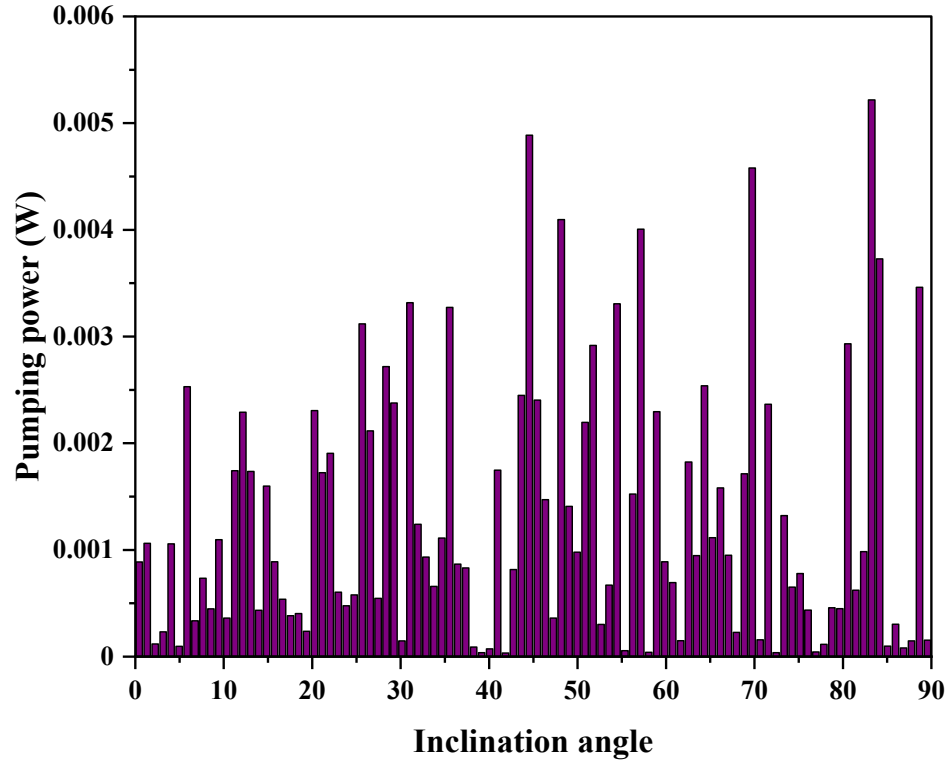

(a)

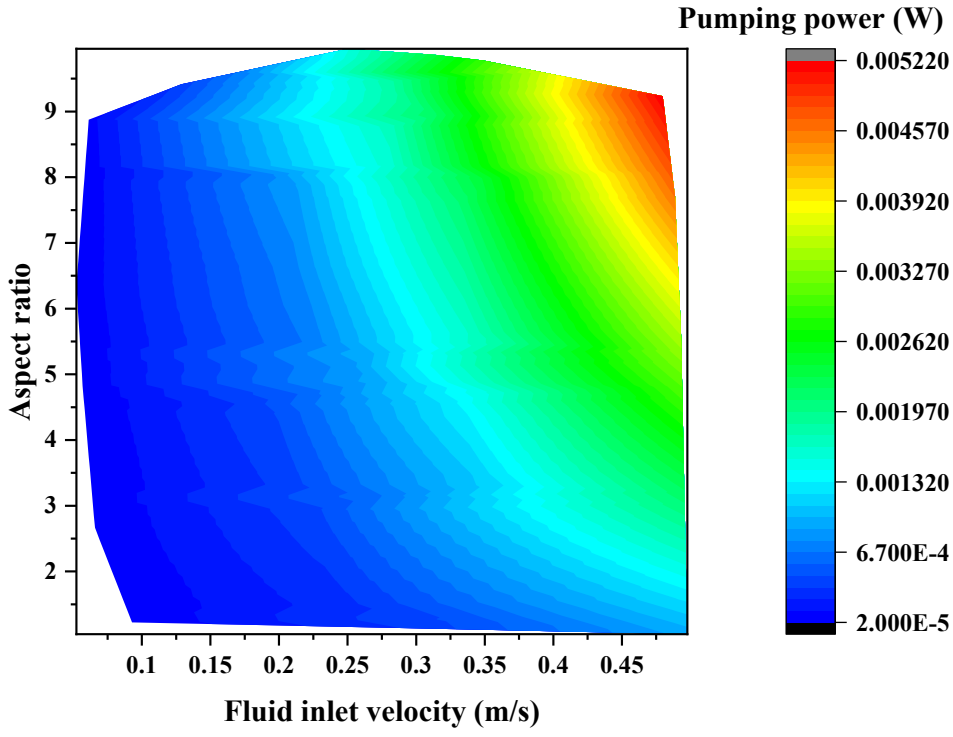

(b)

Fig. 17. Variation of pumping power for input parameters: (a) inclination angle; (b) aspect ratio and fluid inlet velocity.

Fig. 12(b). The temperature in the battery is 301.4 K with a temperature difference of 4.4 K at a fluid inlet temperature of 299.4 K. Thus, the fluid inlet temperature on its own is not sufficient to determine the thermal performance of the mini-channel cooling system. Fig. 12(c) compares the temperature contours for DOEs with fluid inlet temperatures of 312.9 K and 298.1 K. The minimum and maximum temperature difference values are 0.52 K and 6.45 K, respectively, for fluid inlet temperatures of 312.9 K ($i = 5°$) and 298.1 K ($i = 68.9°$). Fig. 13 shows the effect of mass flow rate and fluid inlet temperature on the volume average temperature. The increase in mass flow rate enhances the thermal

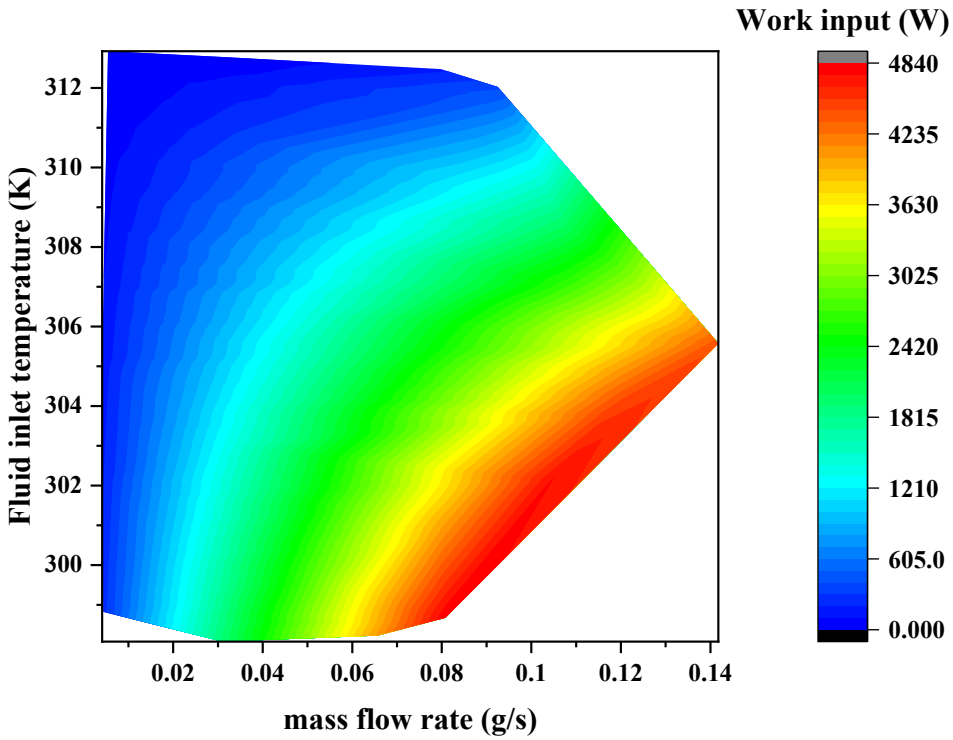

Fig. 18. Variation of work input against mass flow rate and fluid inlet temperature.

performance for low fluid inlet temperature values.

4.3. Effects of mass flow rate, Re, and aspect ratio

The previous section highlighted that fluid inlet temperature can be a determinant input factor in decreasing the volume average temperature of the battery. However, there are other parameters which affect the overall thermal performance of the battery; namely, the temperature difference and the parasitic power consumption (which is directly linked with the pressure drop in the mini-channel). The flow pattern also plays a key role. Fig. 14 shows the counter-flow pattern adopted for this study. The fluid enters and exits at different sides in the mini-channels placed on both surfaces of the battery. This helps in avoiding unnecessary hotspots which would happen if fluid were made to flow in a parallel direction at both planes.

The effects of mass flow rate on the pressure drop across the cell's length and on the volume average temperature in the cell are shown in Fig. 15(a). The values of the volume average temperature for the extremity points are 311.41 K and 307.84 K for mass flow rates of 0.7 g/s and 23.6 g/s, respectively. Although the few data points for higher mass flow rate conditions exhibit, in general, lower volume average temperatures than those for lower mass flow rates, some low mass flow rates result in reduced values of volume average temperature. These instances indicate that other variables involved in the design (such as fluid inlet temperature, inclination angle, and aspect ratio) have similar dominating effects on volume average temperature. It can be thus concluded that mass flow rate on its own is not sufficient to define the thermal performance of the mini-channel cooling system. It is also noted that no typical trend is followed by the pressure drop against mass flow rate. The pressure drop directly affects the parasitic power consumption required for the mini-channel cooling system.

Fig. 15(b) shows the effects that the Reynolds number and the aspect ratio have on the volume average temperature in the cell. These two variables, in combination, can help to intuitively explain several regions of the plot. In this case, increments in their values imply a larger quantity of coolant flows over a wider contact area with the battery surface—in turn, leading to lower volume average temperatures. These are the regions where Re and the aspect ratio determine the thermal performance of the BTMS. However, there are other regions in the plot where these two variables cannot override the effects of other design variables. An example of this is the rise in volume average temperature when Re increases in the ranges 200–600 and 1000–1200 for aspect ratios less than 6. These observations support the idea that other design variables should be considered in conjunction with Re and aspect ratio, through a multi-criteria decision-making process, to select a suitable retrofitting configuration.

Fig. 15(c) compares the temperature contours of the DOEs with similar fluid inlet temperature (309 K) but different aspect ratios (8.2 and 1.1). The DOE with an aspect ratio of 8.2 exhibits fewer hot spots. Additionally, a greater area of the battery is at a lower temperature than for the case of a DOE with an aspect ratio of 1.1.

4.4. Effect of inclination angle

Another important dimensional parameter is the angle at which the mini-channels are inclined on the two planes of the battery. Fig. 16(a) shows the variation of the pressure drop with the inclination angle. The pressure drop was calculated for the cell length. There is no definite trend for the variation and the data points are scattered in the search space unevenly. Fig. 16(b) shows the effect of the inclination angle on the volume average temperature in the battery. It is observed that some values of inclination angle yield a better thermal performance than other design points (e.g. exhibiting a lower temperature difference). The reason behind this behavior for some inclination angles is the better outspread of the mini-channels on the two planes. Fig. 16(c) explains this phenomenon. The contours of volume average temperature are compared with two inclination angles (1.4° and 68.9°) having a similar fluid inlet temperature (298 K). The cooling load is almost the same in the two cases, but the difference in volume average temperature can be observed just due to the difference in the angle at which the mini-channels are inclined.

4.5. Parasitic power consumption

The pumping power varies with the position at which the mini-channels are placed in the battery. Fig. 17(a) shows this variation. It can be noticed that at some values of inclination angle the pumping power required is reduced. These design points can be marked as favorable for the overall performance of the mini-channel cooling system. The least and most amounts of pumping power are required for mini-channels inclined at angles of 41.9° and 83.3°, respectively.

Pumping power is also affected by the fluid inlet velocity and the aspect ratio of the mini-channels. Fig. 17(b) shows the variation of pumping power against fluid inlet velocity and aspect ratio. The pumping power decreases for lower values of aspect ratio and fluid inlet velocity. The least amount of pumping power is required for the design case with a fluid inlet velocity of 0.066 m/s and an aspect ratio of 2.7.

The work input required by the refrigeration cycle is affected by the mass flow rate, the fluid inlet temperature, and the ambient condition. The ambient temperature in this paper is constant at 313 K. The mass flow rate and the fluid inlet temperature were parameterized as design points for the LHS method. Fig. 18 shows the variation of work input required against mass flow rate and fluid inlet temperature. The work input required is less for lower values of both mass flow rate and fluid inlet temperature.

The magnitude of the pumping power is negligible compared to the refrigeration work input required to achieve a low temperature coolant to flow through the mini-channels. The latter, therefore, requires a higher emphasis in the design considerations for an active liquid cooling-based BTMS. To achieve a faster rate of heat extraction from a battery, it is thus more efficient to increase the rate of flow of coolant with a relatively high inlet temperature rather than reducing the inlet temperature to have a low coolant flow rate.

To have an enhanced coolant flow rate, it is further desirable to increase the aspect ratio of the mini-channels rather than increasing the coolant velocity through narrow channels. Larger aspect ratios result in a larger surface area of heat extraction by the coolant from the battery and a broader distribution of the cooling effect over the battery surfaces. This helps in minimizing temperature differences within the battery and leads to a better sustained battery health.

5. Optimal design selection

The 100 design cases vary widely in terms of the key performance markers considered in the study (i.e. volume average temperature, power consumption by the BTMS, and temperature difference). It should be noted that only the refrigeration power required to supply cold liquid coolant at the inlet of the mini-channels (W_c) was considered as the total power consumption, as W_P is substantially lower compared to W_c. An entropy-based TOPSIS was implemented on the dataset consolidating the output parameter values for all the cases. These values and subsequent ranks of the cases obtained from TOPSIS are summarized in Table A in the Appendix. The results suggest that Case 15 is the most suitable considering the 3 judging criteria (with a volume average temperature of 313.31 K, a power consumption by the BTMS of 0.85 W, and a temperature difference of 0.42 K). Conversely, Case 84 is the least suitable design (with a volume average temperature of 304.65 K, a power consumption by the BTMS of 2419.87 W, and a temperature difference of 12.79 K).

Although Case 84 achieves an overall lower battery temperature, there are zones with hotspots that result in a significant difference between the maximum and the minimum temperature. The substantially large cooling power consumption and the large temperature difference indicate a high degree of local cooling near the coolant flow, while leaving distant regions relatively hot. On the other hand, the minimal power consumption and temperature difference exhibited in Case 15 outweigh the relatively hotter volume average temperature being presented.

It should be highlighted that the rankings of different cases may change if one intends to prioritize a single output parameter over the others. For example, if the goal is to minimize only the volume average temperature with little focus on the cooling power requirement and temperature difference, one might opt to choose Case 8, which results in a minimum volume average temperature (301.14 K) — albeit a significant cooling power consumption (965.47 W) and temperature difference (6.46 K).

6. Conclusions

This paper presented a comprehensive analysis of the effects of geometric and thermofluidic parameters on the performance of a liquid coolant-based BTMS for an EV. The battery of the vehicle was simulated with an experimentally validated NTGK model using a realistic driving cycle under hot ambient temperature conditions. The maximum temperature at the end of the driving cycle was 336.95 K.

It was shown that the temperature distribution across the battery significantly depends on the mini-channel inclination angle. Diagonal and vertical mini-channels lead to a more uniform temperature distribution compared to horizontal mini-channels. Heat removal through a very cold fluid flow can lead to a lower volume average temperature of the battery, but it can also trigger undesirable high temperature difference because of intense localized cooling.

Considering the parasitic power consumption of the BTMS, a high coolant flow rate with a relatively high inlet temperature was found to be more efficient than a low coolant flow rate with a relatively cold inlet temperature. The coolant flow rate should preferably be enhanced by increasing the mini-channel aspect ratio than by increasing the fluid velocity. This is because an increased aspect ratio leads to a larger surface area of heat extraction from the battery by the coolant which, in turn, reduces the temperature difference in the battery.

The detrimental effects of high temperature gradients in the battery and high cooling power consumption may not justify a lower volume average temperature obtained in such cases. It would rather be more desirable to achieve a more uniform and less intense cooling with reduced power consumption in the BTMS to strike a balance between battery health and energy economy of the cooling technology. The most suitable case, as suggested by the adopted TOPSIS analysis, resulted in a volume average temperature of 313.31 K, a power consumption by the BTMS of 0.85 W, and a temperature difference of 0.42 K.

Declaration of Competing Interest

The authors declare that they have no known competing financial interests or personal relationships that could have appeared to influence the work reported in this paper.

Data availability

Data will be made available on request.

Acknowledgement

The authors thank IIT Delhi HPC facility for computational resources. Also, the first author extends her gratitude to Mr. Sagar Vashisht, Mr. Tewodros Belay Ashagre, and Mr. Rahul Verma for their help in the experimental study. The authors would also like to offer their sincere thanks to the Department of Science and Technology, Government of India funded project titled “Different Energy Vector Integration for Storage of Energy”, Grant number-TMD/CERI/MICALL19/2020/03 (G) for providing the necessary sources for carrying out the research. The work from the final author was supported in part by FLEXIS—a project part-funded by the European Regional Development Fund (ERDF) through the Welsh Government (WEFO case number 80836).

Appendix A

See Table A1

Table A1
Summary of the input/output parameters for the BTMS design cases and results of TOPSIS.

Case no.	Design input parameters				CFD simulation output			Weight normalized data matrix			TOPSIS output			
	Fluid inlet velocity m/s	Fluid inlet temp. K	Aspect ratio	Inclination angle (degree)	Criteria 1 (Temp.) K	Criteria 2 (Power) W	Criteria 3 (Temp. Difference) K	Criteria 1 (Temp.) K	Criteria 2 (Power) W	Criteria 3 (Temp. Difference) K	Euclidian dist. from ideal solution (S+)	Euclidian dist. from anti-ideal solution (S-)	Performance scores(S-)/[(S+)+(S-)]	Rank
1	0.18275	310.225	3.295	85.95	312.33	84.06	0.31	9.0959E-06	0.00657	0.00127	0.00650	0.18973	0.96687	6
2	0.29075	303.475	1.405	18.45	311.68	204.84	9.20	9.0770E-06	0.01601	0.03749	0.03957	0.17379	0.81456	39
3	0.05675	299.425	4.825	58.05	301.44	220.66	4.44	8.7787E-06	0.01724	0.01808	0.02403	0.17538	0.87948	30
4	0.23225	312.625	2.845	76.05	314.31	12.81	2.87	9.1535E-06	0.00100	0.01168	0.01044	0.19259	0.94856	10
5	0.07025	300.025	7.255	38.25	306.89	422.12	12.10	8.9375E-06	0.03299	0.04929	0.05822	0.15616	0.72843	59
6	0.47075	305.575	8.965	44.55	307.84	2201.12	5.77	8.9653E-06	0.17201	0.02352	0.17337	0.03411	0.16442	96
7	0.21425	312.475	7.795	59.85	314.22	87.66	3.45	9.1510E-06	0.00685	0.01406	0.01447	0.18637	0.92793	15
8	0.46625	298.075	2.755	68.85	301.14	965.47	6.46	8.7701E-06	0.07545	0.02632	0.07943	0.11675	0.59512	75
9	0.11075	301.675	4.645	61.65	306.32	331.97	10.22	8.9209E-06	0.02594	0.04164	0.04795	0.16356	0.77329	49
10	0.08825	301.075	7.975	89.55	304.34	421.99	3.37	8.8633E-06	0.03298	0.01372	0.03518	0.16100	0.82066	38
11	0.15125	298.975	3.655	67.95	303.31	1035.72	5.86	8.8331E-06	0.08094	0.02387	0.08397	0.11203	0.57159	77
12	0.08375	303.925	8.515	30.15	308.31	374.66	8.57	8.9789E-06	0.02928	0.03491	0.04455	0.16085	0.78309	45
13	0.16925	301.825	8.155	24.75	307.47	850.87	10.63	8.9545E-06	0.06649	0.04332	0.07861	0.12299	0.61006	72
14	0.31775	303.775	6.175	66.15	306.43	2256.33	4.77	8.9243E-06	0.17632	0.01942	0.17718	0.03597	0.16875	95
15	0.13325	312.925	1.675	4.95	313.31	0.85	0.42	9.1246E-06	0.00007	0.00169	0.00042	0.19588	0.99787	1
16	0.38975	309.925	3.115	73.35	311.83	194.23	3.51	9.0813E-06	0.01518	0.01430	0.01995	0.17818	0.89932	24
17	0.37625	300.625	6.445	20.25	307.32	1604.24	11.92	8.9499E-06	0.12536	0.04857	0.13393	0.06389	0.32299	91
18	0.27275	309.775	9.595	40.95	311.08	560.59	3.19	9.0596E-06	0.04381	0.01299	0.04528	0.15071	0.76896	51
19	0.07475	305.125	2.215	72.45	311.14	68.07	5.46	9.0613E-06	0.00532	0.02226	0.02163	0.18634	0.89600	26
20	0.06575	308.425	2.665	41.85	312.39	59.84	5.02	9.0977E-06	0.00468	0.02045	0.01972	0.18728	0.90474	23
21	0.16475	304.525	4.195	52.65	308.85	484.91	7.06	8.9947E-06	0.03789	0.02877	0.04677	0.15314	0.76606	53
22	0.39875	307.825	5.635	58.95	311.28	410.23	5.16	9.0653E-06	0.03206	0.02103	0.03760	0.16027	0.80998	41
23	0.48425	309.175	1.135	67.05	312.03	122.49	3.07	9.0871E-06	0.00957	0.01249	0.01470	0.18405	0.92603	16
24	0.09725	302.275	1.855	55.35	307.93	117.49	6.42	8.9678E-06	0.00918	0.02618	0.02652	0.18191	0.87277	33

(*continued on next page*)

Table A1 (*continued*)

Case no.	Design input parameters				CFD simulation output			Weight normalized data matrix			TOPSIS output			
	Fluid inlet velocity m/s	Fluid inlet temp. K	Aspect ratio	Inclination angle (degree)	Criteria 1 (Temp.) K	Criteria 2 (Power) W	Criteria 3 (Temp. Difference) K	Criteria 1 (Temp.) K	Criteria 2 (Power) W	Criteria 3 (Temp. Difference) K	Euclidian dist. from ideal solution (S+)	Euclidian dist. from anti-ideal solution (S-)	Performance scores(S-)/[(S+)+(S-)]	Rank
25	0.33125	299.875	6.265	11.25	306.65	1388.31	11.47	8.9306E-06	0.10849	0.04674	0.11757	0.08086	0.40749	86
26	0.26825	305.275	7.885	49.05	308.18	1252.74	7.11	8.9752E-06	0.09789	0.02897	0.10167	0.09433	0.48126	81
27	0.36725	307.375	7.525	5.85	310.29	785.56	5.06	9.0366E-06	0.06139	0.02063	0.06430	0.13176	0.67203	69
28	0.31325	301.225	9.865	71.55	303.33	1918.36	8.91	8.8338E-06	0.14991	0.03629	0.15388	0.04262	0.21690	93
29	0.49325	298.225	5.545	88.65	302.73	2026.87	13.02	8.8165E-06	0.15839	0.05304	0.16657	0.03071	0.15567	97
30	0.15575	305.725	5.365	6.75	310.24	305.92	5.99	9.0350E-06	0.02391	0.02441	0.03322	0.16766	0.83461	36
31	0.34925	302.125	9.775	51.75	305.20	2372.98	10.28	8.8883E-06	0.18544	0.04190	0.18977	0.01173	0.05822	99
32	0.38075	299.125	4.555	13.05	307.79	1236.45	12.82	8.9638E-06	0.09662	0.05225	0.10918	0.09248	0.45859	83
33	0.19625	306.325	6.805	33.75	309.58	717.28	6.31	9.0158E-06	0.05605	0.02572	0.06109	0.13582	0.68976	65
34	0.40325	309.475	8.245	31.05	311.54	686.14	4.98	9.0729E-06	0.05362	0.02029	0.05683	0.13938	0.71038	61
35	0.16025	306.475	6.985	79.65	308.55	367.47	5.43	8.9858E-06	0.02872	0.02211	0.03542	0.16334	0.82178	37
36	0.11525	300.325	7.165	19.35	306.80	554.95	12.78	8.9350E-06	0.04337	0.05208	0.06675	0.14574	0.68585	66
37	0.43925	304.825	8.605	48.15	307.12	2075.38	5.90	8.9443E-06	0.16218	0.02405	0.16370	0.03957	0.19465	94
38	0.43025	307.075	8.785	57.15	309.05	1337.07	4.68	9.0004E-06	0.10448	0.01907	0.10592	0.09118	0.46260	82
39	0.25475	302.875	2.395	78.75	307.56	316.18	8.14	8.9571E-06	0.02471	0.03317	0.04031	0.16559	0.80423	42
40	0.49775	309.025	1.045	32.85	312.34	106.38	5.13	9.0963E-06	0.00831	0.02092	0.02130	0.18362	0.89604	25
41	0.24575	302.425	3.205	16.65	309.58	435.02	7.83	9.0159E-06	0.03399	0.03191	0.04571	0.15654	0.77399	47
42	0.20075	303.625	8.335	37.35	307.48	1296.42	8.74	8.9547E-06	0.10131	0.03560	0.10690	0.08951	0.45572	84
43	0.32225	300.175	2.125	53.55	304.47	451.73	7.37	8.8671E-06	0.03530	0.03004	0.04549	0.15551	0.77369	48
44	0.10175	310.075	5.995	70.65	311.63	91.86	2.46	9.0757E-06	0.00718	0.01001	0.01126	0.18694	0.94318	11
45	0.36275	311.875	9.685	25.65	312.52	220.10	1.31	9.1016E-06	0.01720	0.00534	0.01761	0.17840	0.91016	21
46	0.32675	312.025	9.055	29.25	312.59	188.63	1.23	9.1037E-06	0.01474	0.00501	0.01514	0.18085	0.92274	17
47	0.42125	301.975	2.935	46.35	306.36	947.21	7.22	8.9221E-06	0.07402	0.02941	0.07912	0.11748	0.59755	74
48	0.30425	298.375	5.185	31.95	302.67	1366.98	10.28	8.8148E-06	0.10682	0.04187	0.11421	0.08303	0.42095	85
49	0.12425	311.725	5.905	3.15	312.73	46.91	1.25	9.1077E-06	0.00367	0.00511	0.00526	0.19153	0.97328	5

(*continued on next page*)

Table A1 (*continued*)

Case no.	Design input parameters				CFD simulation output			Weight normalized data matrix			TOPSIS output			
	Fluid inlet velocity m/s	Fluid inlet temp. K	Aspect ratio	Inclination angle (degree)	Criteria 1 (Temp.) K	Criteria 2 (Power) W	Criteria 3 (Temp. Difference) K	Criteria 1 (Temp.) K	Criteria 2 (Power) W	Criteria 3 (Temp. Difference) K	Euclidian dist. from ideal solution (S+)	Euclidian dist. from anti-ideal solution (S-)	Performance scores(S-)/[(S+)+(S-)]	Rank
50	0.05225	307.525	6.355	76.95	310.89	93.48	4.63	9.0541E-06	0.00730	0.01885	0.01901	0.18498	0.90681	22
51	0.09275	298.825	1.225	39.15	307.08	130.32	7.26	8.9431E-06	0.01018	0.02957	0.03005	0.18045	0.85723	35
52	0.35375	301.375	6.715	26.55	306.76	1543.82	10.96	8.9338E-06	0.12064	0.04465	0.12814	0.06897	0.34991	90
53	0.42575	305.875	3.475	21.15	310.33	570.52	5.70	9.0376E-06	0.04458	0.02322	0.04963	0.14756	0.74832	57
54	0.33575	311.425	3.565	9.45	312.69	95.36	1.39	9.1065E-06	0.00745	0.00568	0.00860	0.18772	0.95620	9
55	0.17825	308.725	4.285	47.25	311.54	223.41	4.71	9.0730E-06	0.01746	0.01921	0.02498	0.17494	0.87504	32
56	0.22325	299.275	4.105	27.45	308.42	709.64	12.53	8.9822E-06	0.05545	0.05105	0.07447	0.13366	0.64219	70
57	0.38525	304.675	6.535	43.65	308.18	1523.36	7.59	8.9751E-06	0.11904	0.03093	0.12261	0.07347	0.37467	88
58	0.34475	306.775	9.325	28.35	308.44	1059.82	5.32	8.9827E-06	0.08282	0.02168	0.08523	0.11081	0.56524	78
59	0.21875	308.275	5.005	81.45	309.87	261.82	2.03	9.0244E-06	0.02046	0.00826	0.02156	0.17448	0.89004	28
60	0.48875	307.225	7.705	69.75	308.33	1098.75	2.44	8.9794E-06	0.08586	0.00994	0.08623	0.11188	0.56473	79
61	0.06125	303.175	8.875	86.85	306.45	268.91	8.27	8.9248E-06	0.02101	0.03371	0.03861	0.16919	0.81420	40
62	0.27725	299.575	3.745	75.15	303.98	704.72	7.93	8.8528E-06	0.05507	0.03230	0.06315	0.13563	0.68231	68
63	0.26375	303.025	4.915	15.75	308.91	671.26	8.35	8.9964E-06	0.05246	0.03401	0.06178	0.13796	0.69071	64
64	0.45725	308.125	5.455	80.55	309.65	616.92	2.11	9.0180E-06	0.04821	0.00859	0.04869	0.14774	0.75210	55
65	0.17375	310.675	8.065	22.95	311.97	177.02	2.30	9.0856E-06	0.01383	0.00937	0.01597	0.18062	0.91876	19
66	0.43475	304.225	6.895	35.55	306.98	2215.59	6.68	8.9403E-06	0.17314	0.02723	0.17501	0.03035	0.14778	98
67	0.29525	299.725	7.345	14.85	306.01	1493.56	12.00	8.9119E-06	0.11671	0.04891	0.12600	0.07250	0.36526	89
68	0.47525	309.625	5.725	54.45	311.22	462.07	3.64	9.0636E-06	0.03611	0.01485	0.03851	0.15769	0.80370	43
69	0.24125	300.775	2.575	13.95	304.88	395.97	8.30	8.8791E-06	0.03094	0.03384	0.04488	0.15932	0.78023	46
70	0.47975	308.575	9.235	83.25	310.04	990.55	2.36	9.0294E-06	0.07741	0.00963	0.07779	0.11983	0.60637	73
71	0.34025	310.375	7.615	50.85	312.89	164.97	0.86	9.1124E-06	0.01289	0.00348	0.01301	0.18304	0.93362	13
72	0.14675	312.325	8.425	8.55	312.89	42.42	0.86	9.1124E-06	0.00331	0.00348	0.00393	0.19228	0.97997	4
73	0.45275	308.875	4.735	64.35	311.83	492.81	6.49	9.0813E-06	0.03851	0.02646	0.04596	0.15292	0.76890	52
74	0.12875	302.575	9.415	17.55	307.38	663.32	9.56	8.9520E-06	0.05183	0.03894	0.06402	0.13799	0.68309	67

(*continued on next page*)

Table A1 (*continued*)

Case no.	Design input parameters				CFD simulation output			Weight normalized data matrix			TOPSIS output			
	Fluid inlet velocity m/s	Fluid inlet temp. K	Aspect ratio	Inclination angle (degree)	Criteria 1 (Temp.) K	Criteria 2 (Power) W	Criteria 3 (Temp. Difference) K	Criteria 1 (Temp.) K	Criteria 2 (Power) W	Criteria 3 (Temp. Difference) K	Euclidian dist. from ideal solution (S +)	Euclidian dist. from anti-ideal solution (S-)	Performance scores(S-)/[(S +)+(S-)]	Rank
75	0.29975	312.775	4.465	4.05	313.21	15.08	0.39	9.1215E-06	0.00118	0.00157	0.00115	0.19484	0.99413	2
76	0.25025	305.425	9.955	56.25	307.86	946.90	8.00	8.9658E-06	0.07399	0.03258	0.08029	0.11691	0.59286	76
77	0.22775	304.375	8.695	34.65	307.58	1109.01	8.19	8.9575E-06	0.08666	0.03336	0.09235	0.10431	0.53041	80
78	0.14225	309.325	2.485	87.75	312.31	65.54	2.01	9.0954E-06	0.00512	0.00819	0.00857	0.18937	0.95672	8
79	0.23675	311.275	3.025	23.85	312.73	68.26	1.34	9.1075E-06	0.00533	0.00546	0.00673	0.18983	0.96578	7
80	0.40775	301.525	1.585	36.45	306.53	466.58	7.25	8.9271E-06	0.03646	0.02956	0.04609	0.15444	0.77015	50
81	0.44375	310.525	1.495	82.35	315.92	84.11	3.90	9.2005E-06	0.00657	0.01587	0.01598	0.18627	0.92099	18
82	0.41225	298.525	2.035	1.35	309.26	613.05	8.86	9.0067E-06	0.04791	0.03610	0.05918	0.14221	0.70615	62
83	0.25925	304.075	3.835	60.75	310.16	517.94	7.35	9.0329E-06	0.04047	0.02996	0.04955	0.15041	0.75218	54
84	0.39425	298.675	6.085	45.45	304.65	2419.87	12.79	8.8722E-06	0.18910	0.05210	0.19575	0.00094	0.00479	100
85	0.41675	310.975	1.765	49.95	315.33	96.59	6.91	9.1835E-06	0.00755	0.02817	0.02792	0.18325	0.86778	34
86	0.10625	306.025	3.925	2.25	311.02	146.83	5.00	9.0579E-06	0.01147	0.02037	0.02224	0.18061	0.89035	27
87	0.30875	302.725	3.385	0.45	309.61	540.43	7.42	9.0168E-06	0.04223	0.03023	0.05115	0.14863	0.74396	58
88	0.20975	310.825	6.625	7.65	311.04	153.39	1.96	9.0583E-06	0.01199	0.00800	0.01369	0.18275	0.93033	14
89	0.07925	311.125	4.375	40.05	312.29	42.84	3.51	9.0949E-06	0.00335	0.01430	0.01343	0.18975	0.93391	12
90	0.46175	307.675	4.015	12.15	311.14	504.12	4.26	9.0614E-06	0.03939	0.01737	0.04250	0.15390	0.78362	44
91	0.20525	304.975	9.145	63.45	308.79	843.81	7.69	8.9929E-06	0.06594	0.03132	0.07240	0.12506	0.63333	71
92	0.44825	300.925	7.435	84.15	302.53	2030.60	2.36	8.8107E-06	0.15868	0.00962	0.15883	0.05301	0.25025	92
93	0.13775	306.925	1.945	77.85	312.07	81.77	5.71	9.0885E-06	0.00639	0.02327	0.02289	0.18512	0.88996	29
94	0.19175	303.325	7.075	74.25	306.81	673.45	7.15	8.9353E-06	0.05263	0.02913	0.05949	0.13855	0.69962	63
95	0.18725	307.975	9.505	42.75	309.96	659.22	4.79	9.0268E-06	0.05151	0.01952	0.05459	0.14161	0.72177	60
96	0.37175	311.575	5.095	62.55	314.36	139.42	5.84	9.1550E-06	0.01089	0.02379	0.02499	0.18059	0.87845	31
97	0.11975	306.175	2.305	85.05	310.35	94.55	3.98	9.0384E-06	0.00739	0.01621	0.01664	0.18541	0.91766	20
98	0.28175	312.175	1.315	10.35	313.16	15.39	0.53	9.1201E-06	0.00120	0.00217	0.00145	0.19466	0.99261	3
99	0.35825	300.475	5.815	22.05	306.83	1407.27	10.88	8.9357E-06	0.10997	0.04433	0.11804	0.07961	0.40278	87

(*continued on next page*)

Table A1 (*continued*)

Case no.	Design input parameters				CFD simulation output			Weight normalized data matrix			TOPSIS output			
	Fluid inlet velocity m/s	Fluid inlet temp. K	Aspect ratio	Inclination angle (degree)	Criteria 1 (Temp.) K	Criteria 2 (Power) W	Criteria 3 (Temp. Difference) K	Criteria 1 (Temp.) K	Criteria 2 (Power) W	Criteria 3 (Temp. Difference) K	Euclidian dist. from ideal solution (S+)	Euclidian dist. from anti-ideal solution (S-)	Performance scores(S-)/ [(S+)+(S-)]	Rank
100	0.28625	306.625	5.275	65.25	309.81	533.37	7.02	9.0226E-06	0.04168	0.02862	0.04980	0.14943	0.75005	56
Ideal soln.:								8.7701E-06	0.00007	0.001274				
Anti-ideal soln.:								9.2005E-06	0.1891	0.05304				

References

[1] Goal 7 | Department of Economic and Social Affairs. https://sdgs.un.org/goals/goal7 (accessed April 27, 2022).

[2] Wu Z, Wang C, Wolfram P, Zhang Y, Sun X, Hertwich E. Assessing electric vehicle policy with region-specific carbon footprints. Appl Energy 2019;256:113923. https://doi.org/10.1016/J.APENERGY.2019.113923.

[3] Ma S, Jiang M, Tao P, Song C, Wu J, Wang J, et al. Temperature effect and thermal impact in lithium-ion batteries: a review. Prog Nat Sci: Mater Int 2018;28:653–66. https://doi.org/10.1016/J.PNSC.2018.11.002.

[4] Ramadass P, Haran B, White R, Popov BN. Capacity fade of Sony 18650 cells cycled at elevated temperatures: Part II. Capacity fade analysis. J Power Sources 2002; 112:614–20. https://doi.org/10.1016/S0378-7753(02)00473-1.

[5] Chen J, Kang S, E J, Huang Z, Wei K, Zhang B, et al. Effects of different phase change material thermal management strategies on the cooling performance of the power lithium ion batteries: a review. J Power Sources 2019;442:227228. https://doi.org/10.1016/J.JPOWSOUR.2019.227228.

[6] Wright DR, Garcia-Araez N, Owen JR. Review on high temperature secondary Li-ion batteries. Energy Procedia 2018;151:174–81. https://doi.org/10.1016/J.EGYPRO.2018.09.044.

[7] Lu Z, Yu XL, Wei LC, Cao F, Zhang LY, Meng XZ, et al. A comprehensive experimental study on temperature-dependent performance of lithium-ion battery. Appl Therm Eng 2019;158:113800. https://doi.org/10.1016/J.APPLTHERMALENG.2019.113800.

[8] Kim J, Oh J, Lee H. Review on battery thermal management system for electric vehicles. Appl Therm Eng 2019;149:192–212. https://doi.org/10.1016/J.APPLTHERMALENG.2018.12.020.

[9] Cho HM, Choi WS, Go JY, Bae SE, Shin HC. A study on time-dependent low temperature power performance of a lithium-ion battery. J Power Sources 2012; 198:273–80. https://doi.org/10.1016/J.JPOWSOUR.2011.09.111.

[10] Safdari M, Ahmadi R, Sadeghzadeh S. Numerical and experimental investigation on electric vehicles battery thermal management under New European Driving Cycle. Appl Energy 2022;315:119026. https://doi.org/10.1016/J.APENERGY.2022.119026.

[11] Cho I, Park S, Kim J. A fire risk assessment method for high-capacity battery packs using interquartile range filter. J Energy Storage 2022;50:104663. https://doi.org/10.1016/J.EST.2022.104663.

[12] Roe C, Feng X, White G, Li R, Wang H, Rui X, et al. Immersion cooling for lithium-ion batteries – a review. J Power Sources 2022;525:231094. https://doi.org/10.1016/J.JPOWSOUR.2022.231094.

[13] Khateeb SA, Farid MM, Selman JR, Al-Hallaj S. Design and simulation of a lithium-ion battery with a phase change material thermal management system for an electric scooter. J Power Sources 2004;128:292–307. https://doi.org/10.1016/J.JPOWSOUR.2003.09.070.

[14] Al-Hallaj S, Selman JR. Thermal modeling of secondary lithium batteries for electric vehicle/hybrid electric vehicle applications. J Power Sources 2002;110: 341–8. https://doi.org/10.1016/S0378-7753(02)00196-9.

[15] Li WQ, Qu ZG, He YL, Tao YB. Experimental study of a passive thermal management system for high-powered lithium ion batteries using porous metal foam saturated with phase change materials. J Power Sources 2014;255:9–15. https://doi.org/10.1016/J.JPOWSOUR.2014.01.006.

[16] Goli P, Legedza S, Dhar A, Salgado R, Renteria J, Balandin AA. Graphene-enhanced hybrid phase change materials for thermal management of Li-ion batteries. J Power Sources 2014;248:37–43. https://doi.org/10.1016/J.JPOWSOUR.2013.08.135.

[17] Verma A, Rakshit D. Performance analysis of PCM-fin combination for heat abatement of Li-ion battery pack in electric vehicles at high ambient temperature. Therm Sci Eng Progr 2022;32:101314. https://doi.org/10.1016/J.TSEP.2022.101314.

[18] Verma A, Shashidhara S, Rakshit D. A comparative study on battery thermal management using phase change material (PCM). Therm Sci Eng Progr 2019;11: 74–83. https://doi.org/10.1016/J.TSEP.2019.03.003.

[19] Verma A, Saikia P, Rakshit D. Unification of intensive and extensive properties of the passive cooling system under a single envelope for the thermal management of Li-ion batteries. J Energy Storage 2022;50:104184. https://doi.org/10.1016/J.EST.2022.104184.

[20] Kizilel R, Lateef A, Sabbah R, Farid MM, Selman JR, Al-Hallaj S. Passive control of temperature excursion and uniformity in high-energy Li-ion battery packs at high current and ambient temperature. J Power Sources 2008;183:370–5. https://doi.org/10.1016/J.JPOWSOUR.2008.04.050.

[21] Ling Z, Cao J, Zhang W, Zhang Z, Fang X, Gao X. Compact liquid cooling strategy with phase change materials for Li-ion batteries optimized using response surface methodology. Appl Energy 2018;228:777–88. https://doi.org/10.1016/J.APENERGY.2018.06.143.

[22] Pesaran AA, Burch S, Keyser M. An Approach for Designing Thermal Management Systems for Electric and Hybrid Vehicle Battery Packs Preprint 1999.

[23] Meyer J, Agathocleous N, Youmans H, Williams H, Vespa T, Rugh J, et al. Advanced Climate System for EV Extended Range 2017. https://doi.org/10.2172/1413671.

[24] Pesaran AA. Battery Thermal Management in EVs and HEVs: Issues and Solutions. Battery Man. 2001;43.

[25] Chen K, Li X. Accurate determination of battery discharge characteristics – a comparison between two battery temperature control methods. J Power Sources 2014;247:961–6. https://doi.org/10.1016/J.JPOWSOUR.2013.09.060.

[26] Akbarzadeh M, Kalogiannis T, Jaguemont J, Jin L, Behi H, Karimi D, et al. A comparative study between air cooling and liquid cooling thermal management

systems for a high-energy lithium-ion battery module. Appl Therm Eng 2021;198:117503. https://doi.org/10.1016/J.APPLTHERMALENG.2021.117503.
[27] Liu Z, Ivanco A, Onori S. Aging characterization and modeling of nickel-manganese-cobalt lithium-ion batteries for 48V mild hybrid electric vehicle applications. J Energy Storage 2019;21:519–27. https://doi.org/10.1016/J.EST.2018.11.016.
[28] Jahanbakhshi A, Nadooshan AA, Bayareh M. Cooling of a lithium-ion battery using microchannel heatsink with wavy microtubes in the presence of nanofluid. J Energy Storage 2022;49:104128. https://doi.org/10.1016/J.EST.2022.104128.
[29] A Guide to Understanding Battery Specifications, 2008. http://web.mit.edu/evt/summary_battery_specifications.pdf (accessed November 27, 2022).
[30] Qomi ME, Sheikhzadeh GA, Fattahi A. On the micro-scale battery cooling with a sinusoidal hybrid nanofluid flow. J Energy Storage 2022;46:103819. https://doi.org/10.1016/J.EST.2021.103819.
[31] Zhang H, Li C, Zhang R, Lin Y, Fang H. Thermal analysis of a 6s4p Lithium-ion battery pack cooled by cold plates based on a multi-domain modeling framework. Appl Therm Eng 2020;173:115216. https://doi.org/10.1016/J.APPLTHERMALENG.2020.115216.
[32] Monika K, Chakraborty C, Roy S, Dinda S, Singh SA, Datta SP. Parametric investigation to optimize the thermal management of pouch type lithium-ion batteries with mini-channel cold plates. Int J Heat Mass Transf 2021;164:120568. https://doi.org/10.1016/J.IJHEATMASSTRANSFER.2020.120568.
[33] Ran Y, Su Y, Chen L, Yan K, Yang C, Zhao Y. Investigation on thermal performance of water-cooled Li-ion cell and module with tree-shaped channel cold plate. J Energy Storage 2022;50:104040. https://doi.org/10.1016/J.EST.2022.104040.
[34] Amalesh T, Narasimhan NL. Introducing new designs of minichannel cold plates for the cooling of Lithium-ion batteries. J Power Sources 2020;479:228775. https://doi.org/10.1016/J.JPOWSOUR.2020.228775.
[35] Kong W, Zhu K, Lu X, Jin J, Ni M. Enhancement of lithium-ion battery thermal management with the divergent-shaped channel cold plate. J Energy Storage 2021;42:103027. https://doi.org/10.1016/J.EST.2021.103027.
[36] Angani A, Kim H-W, Myeong hwan H, Eugene K, Kyoung-Min K, Rok Cha H. A comparison between Zig-Zag plated hybrid parallel pipe and liquid cooling battery thermal management systems for Lithium-ion battery module. Appl Therm Eng 2023;219:119599. https://doi.org/10.1016/J.APPLTHERMALENG.2022.119599.
[37] Akkaldevi C, Chitta SD, Jaidi J, Panchal S, Fowler M, Fraser R. Coupled Electrochemical-Thermal Simulations and Validation of Minichannel Cold-Plate Water-Cooled Prismatic 20 Ah LiFePO4 Battery. Electrochem 2021, Vol 2, Pages 643-663 2021;2:643–63. https://doi.org/10.3390/ELECTROCHEM2040040.
[38] Chen Y, Chen K, Dong Y, Wu X. Bidirectional symmetrical parallel mini-channel cold plate for energy efficient cooling of large battery packs. Energy 2022;242:122553. https://doi.org/10.1016/J.ENERGY.2021.122553.
[39] Jarrett A, Kim IY. Design optimization of electric vehicle battery cooling plates for thermal performance. J Power Sources 2011;196:10359–68. https://doi.org/10.1016/J.JPOWSOUR.2011.06.090.
[40] Jang DS, Yun S, Hong SH, Cho W, Kim Y. Performance characteristics of a novel heat pipe-assisted liquid cooling system for the thermal management of lithium-ion batteries. Energy Convers Manag 2022;251:115001. https://doi.org/10.1016/J.ENCONMAN.2021.115001.
[41] Guo R, Li L. Heat dissipation analysis and optimization of lithium-ion batteries with a novel parallel-spiral serpentine channel liquid cooling plate. Int J Heat Mass Transf 2022;189:122706. https://doi.org/10.1016/J.IJHEATMASSTRANSFER.2022.122706.
[42] Xu H, Zhang X, Xiang G, Li H. Optimization of liquid cooling and heat dissipation system of lithium-ion battery packs of automobile. Case Stud Therm Eng 2021;26:101012. https://doi.org/10.1016/J.CSITE.2021.101012.
[43] Ding Y, Ji H, Wei M, Liu R. Effect of liquid cooling system structure on lithium-ion battery pack temperature fields. Int J Heat Mass Transf 2022;183:122178. https://doi.org/10.1016/J.IJHEATMASSTRANSFER.2021.122178.
[44] Ding Y, Wei M, Liu R. Channel parameters for the temperature distribution of a battery thermal management system with liquid cooling. Appl Therm Eng 2021;186:116494. https://doi.org/10.1016/j.applthermaleng.2020.116494.
[45] Liu J, Fan Y, Xie Q. Feasibility study of a novel oil-immersed battery cooling system: Experiments and theoretical analysis. Appl Therm Eng 2022;208:118251. https://doi.org/10.1016/J.APPLTHERMALENG.2022.118251.
[46] Zhang F, Zhai L, Zhang L, Yi M, Du B, Li S. A novel hybrid battery thermal management system with fins added on and between liquid cooling channels in composite phase change materials. Appl Therm Eng 2022;207:118198. https://doi.org/10.1016/J.APPLTHERMALENG.2022.118198.
[47] Xin Q, Xiao J, Yang T, Zhang H, Long X. Thermal management of lithium-ion batteries under high ambient temperature and rapid discharging using composite PCM and liquid cooling. Appl Therm Eng 2022;210:118230. https://doi.org/10.1016/J.APPLTHERMALENG.2022.118230.
[48] Jithin Kv, Rajesh PK. Numerical analysis of single-phase liquid immersion cooling for lithium-ion battery thermal management using different dielectric fluids. Int J Heat Mass Transf 2022;188:122608. https://doi.org/10.1016/J.IJHEATMASSTRANSFER.2022.122608.
[49] Amalesh T, Lakshmi NN. Liquid cooling vs hybrid cooling for fast charging lithium-ion batteries: A comparative numerical study. Appl Therm Eng 2022;208:118226. https://doi.org/10.1016/J.APPLTHERMALENG.2022.118226.
[50] Heat Wave Across Europe Sparks Wildfires And Heat-Related Deaths. https://www.forbes.com/sites/carlieporterfield/2022/07/17/heat-wave-across-europe-sparks-wildfires-and-heat-related-deaths/?sh=4e2667ec597e (accessed December 1, 2022).
[51] Canada heat wave: More than 230 deaths reported in British Columbia amid historic heat wave | CNN. https://edition.cnn.com/2021/06/29/americas/canada-heat-wave-deaths/index.html (accessed December 1, 2022).
[52] Hauz Khas, Delhi temperature map | Microsoft Weather. https://www.msn.com/en-in/weather/maps/temperature/in-Hauz-Khas,Delhi?loc=eyJsIjoiSGF1eiBLaGFzIiwiciI6IkRlbGhpIiwicjIiOiJOZXcgRGVsaGkiLCJjIjoiSW5kaWEiLCJpIjoiSU4iLCJ0IjoxMDIsImciOiJlbi1pbiIsIngiOiI3Ny4yMDE4IiwieSI6IjI4LjU1MjYifQ%3D%3D&weadegreetype=C&ocid=winp1taskbar&zoom=5&cvid=ea51bba6cfc74547d002995dcafc1c29# (accessed April 14, 2022).
[53] Wang N, Li C, Li W, Chen X, Li Y, Qi D. Heat dissipation optimization for a serpentine liquid cooling battery thermal management system: An application of surrogate assisted approach. J Energy Storage 2021;40:102771. https://doi.org/10.1016/J.EST.2021.102771.
[54] Li W, Xiao M, Peng X, Garg A, Gao L. A surrogate thermal modeling and parametric optimization of battery pack with air cooling for EVs. Appl Therm Eng 2019;147:90–100. https://doi.org/10.1016/J.APPLTHERMALENG.2018.10.060.
[55] McKay MD, Beckman RJ, Conover WJ. Comparison of Three Methods for Selecting Values of Input Variables in the Analysis of Output from a Computer Code. Http://DxDoiOrg/101080/00401706197910489755 2012;21:239–45. https://doi.org/10.1080/00401706.1979.10489755.
[56] Latin Hypercube Sampling. https://mathieu.fenniak.net/latin-hypercube-sampling/ (accessed November 26, 2022).
[57] Keedwell AD, Dénes J. The concept of orthogonality. Latin Squares and Their Applications 2015:159–203. https://doi.org/10.1016/B978-0-444-63555-6.50005-2.
[58] Shah R, London A. Laminar flow forced convection in ducts. 1978. https://doi.org/10.1016/C2013-0-06152-X.
[59] Chen F, Huang R, Wang C, Yu X, Liu H, Wu Q, et al. Air and PCM cooling for battery thermal management considering battery cycle life. Appl Therm Eng 2020;173:115154. https://doi.org/10.1016/J.APPLTHERMALENG.2020.115154.
[60] Saikia P, Rakshit D, Narayanaswamy R, Wang F, Udayraj. Energy performance and indoor airflow analysis of a healthcare ward designed with resource conservation objectives. Journal of Building Engineering 2021;44:103296. https://doi.org/10.1016/J.JOBE.2021.103296.
[61] Das D, Sharma RK, Saikia P, Rakshit D. An integrated entropy-based multi-attribute decision-making model for phase change material selection and passive thermal management. Decision Anal J 2021;1:100011. https://doi.org/10.1016/J.DAJOUR.2021.100011.
[62] Zhang Y. TOPSIS Method Based on Entropy Weight for Supplier Evaluation of Power Grid Enterprise. Proceedings of the 2015 International Conference on Education Reform and Modern Management 2015;15:334–7. https://doi.org/10.2991/ERMM-15.2015.88.
[63] Liu Y, Liao YG, Lai M-C. Transient Temperature Distributions on Lithium-Ion Polymer SLI Battery. Vehicles 2019, Vol 1, Pages 127-137 2019;1:127–37. https://doi.org/10.3390/VEHICLES1010008.
[64] Panchal S, Dincer I, Agelin-Chaab M, Fraser R, Fowler M. Transient electrochemical heat transfer modeling and experimental validation of a large sized LiFePO4/graphite battery. Int J Heat Mass Transf 2017;109:1239–51. https://doi.org/10.1016/j.ijheatmasstransfer.2017.03.005.
[65] Hu X, Johannesson L, Murgovski N, Egardt B. Longevity-conscious dimensioning and power management of the hybrid energy storage system in a fuel cell hybrid electric bus. Appl Energy 2015;137:913–24. https://doi.org/10.1016/J.APENERGY.2014.05.013.
[66] Celik A, Coban H, Göcmen S, Ezan MA, Gören A, Erek A. Passive thermal management of the lithium-ion battery unit for a solar racing car. Int J Energy Res 2019;43:3681–91. https://doi.org/10.1002/ER.4521.
[67] Song M, Choe SY. Parameter sensitivity analysis of a reduced-order electrochemical-thermal model for heat generation rate of lithium-ion batteries. Appl Energy 2022;305:117920. https://doi.org/10.1016/J.APENERGY.2021.117920.
[68] SVD-ROM for Battery Thermal Management Products Used: Ansys Fluent Ansys Twin Builder 2020.
[69] Shah RK, London AL. Rectangular ducts. Laminar Flow Forced Convection in Ducts 1978:196–222. https://doi.org/10.1016/B978-0-12-020051-1.50012-7.
[70] Talluri T, Kim TH, Shin KJ. Analysis of a Battery Pack with a Phase Change Material for the Extreme Temperature Conditions of an Electrical Vehicle. Energies 2020, Vol 13, Page 507 2020;13:507. https://doi.org/10.3390/EN13030507.